DEVELOPING AN ACTIVE, HIGH-HEAT-FLUX THERMAL MANAGEMENT STRATEGY FOR POWER ELECTRONICS VIA JUMPING-DROPLET PHASE-CHANGE COOLING

BY

THOMAS PETER FOULKES

THESIS

Submitted in partial fulfillment of the requirements
for the degree of Master of Science in Electrical and Computer Engineering
in the Graduate College of the
University of Illinois at Urbana-Champaign, 2017

Urbana, Illinois

Advisers:

Assistant Professor Robert Pilawa-Podgurski
Assistant Professor Nenad Miljkovic

ABSTRACT

Mitigating heat generated by hot spots inside of power electronic devices is a formidable obstacle to further increases in power density. This work presents the first demonstration of active cooling for hot spots in compact electronics via electric-field-enhanced (EFE) jumping-droplet condensation. To test the viability of EFE condensation for electronic hot spot cooling, an experimental setup was developed to remove heat via droplet evaporation from single and multiple high-power gallium nitride (GaN) transistors acting as local hot spots (4.6 mm x 2.6 mm). An externally powered circuit was developed to direct jumping droplets from a copper oxide (CuO) nanostructured superhydrophobic surface to the transistor hot spots by applying electric fields between the condensing surface and an electrically floated circuit (directly to the transistor) or a guard ring (surrounding the transistor). Heat transfer measurements were performed in ambient air (22-25 °C air temperature, 20-45% relative humidity) to determine the effect of gap spacing (1-5 mm) between the GaN transistor and superhydrophobic surface, strength of the electric field (50-250 V/cm), and the cooling performance at different applied heat flux conditions (demonstrated to 13 W/cm^2) along with power dissipation levels ($\approx$ 1.57 W). EFE condensation was shown to enhance the heat transfer from the local hot spot by $\approx$ 200% compared to cooling without jumping and by 20% compared to non-EFE jumping. Dynamic switching of the electric field for a two-GaN system reveals the potential for active cooling of mobile hot spots. The opportunity for further cooling enhancement by the removal of non-condensable gases (NCGs) is discussed, promising local hot spot heat dissipation rates approaching 120 W/cm^2. This work not only demonstrates EFE-condensation-based electronics cooling for the first time, but also provides a framework for the development of active jumping-droplet-based vapor chambers and heat pipes capable of spatial and temporal thermal dissipation control.

To:

My parents, Jim and Beth Foulkes, for their unconditional love, sage advice, and inspiration to be persistent and to ask questions.

Dr. Herbert Bailey, who gave me the greatest deal in history by bartering his expertise with the sport of racquetball and his wisdom about the exciting, curious world of mathematics for help with his yard work.

ACKNOWLEDGMENTS

I want to thank Professors Robert Pilawa-Podgurski and Nenad Miljkovic for their mentorship and technical guidance throughout this project. In addition to serving as ideal examples of what it truly means to collaborate, they have also helped me expand my horizons to become more "T-Shaped" by working at the intersection of advanced heat transfer, surface science, packaging, circuit design, control, and the future. I am immensely thankful for this opportunity to collaborate on this and many other inspirational and exciting research endeavors at the bleeding edge of what is possible.

Moreover, I want to thank Dr. Tomas Modeer, the post-doc researcher in the Pilawa group, for his willingness to collaborate on the NASA project, to share his insights about the modeling and optimization of power electronics, and to engage in cultural exchange. I have learned a great deal from his unique engineering perspective. I also want to acknowledge the technical mentorship that I have received from the senior members of the Pilawa research group: Yutian Lei, Shibin Qin, Andrew Stillwell, Enver Candan, Pourya Assem, and Chris Barth, as well as the lifetime friendships that I have forged with the entire Pilawa group and graduate students from the Power & Energy area for the ECE department. To paraphrase Newton, "If I have seen further, it is only because I have had the opportunity to stand on the shoulders of these giants."

I want to express sincere thanks to my collaborators who contributed significantly to various phases of this jumping-droplets heat transfer work from the Mechanical Science and Engineering Department at the University of Illinois at Urbana-Champaign: Junho Oh, Patrick Birbarah, Jesus Sotelo, Longnan Li, and Keith Coulson; and from Sandia National Laboratory: Dr. Jason Neely and Dr. Bob Kaplar. Specifically, Junho Oh and Patrick Birbarah collaborated with me to obtain the measurements and to develop the models of the ambient heat transfer behavior discussed in this thesis. I am

grateful for their insightful contributions and camaraderie during the long hours in the laboratory. I also want to acknowledge the contributions of the undergraduate researchers: Sabrina Yin helped with the heat transfer measurement process, and Michelle Rentauskas worked on the thermographic liquid crystal imaging process. Together, we have realized a new paradigm of power electronics cooling, which has been recognized with a best presentation award at the 2017 IEEE Applied Power Electronics Conference.

I would be remiss if I did not thank my mentors from my internships, from my hometown, and from Rose-Hulman Institute of Technology without whom I would not have pursued graduate study. Undoubtedly, my two summers at Delphi Electronics and Safety in Kokomo, Indiana, had a profoundly positive impact on my desire to pursue a career in research and design. The kindness and friendly atmosphere at Delphi was truly special and enabled me to learn from a wide variety of challenging and meaningful projects. Specifically, sage advice from Ralph Taylor, Brian Denta, Kwan Shim, and Yansong Chen was instrumental in my decision to pursue graduate study in the cross-disciplinary field of power electronics. Moreover, I am appreciative of the career advice and technical development opportunities made available to me during an internship at NASA Glenn Research Center by Ralph Jansen, Cheryl Bowman, Randy Bowman, and David Avanesian. This propelled me into my second year of graduate studies.

Similarly, I received a fantastic foundation in technical communication and critical thinking during my high school education. I would like to thank Julia Thistle and Katherine Utley for developing a world-class language arts and honors writing program. Throughout my Science Fair career, I received advice, guidance, and inspiration from many wonderful educators including: Glenn Cook, Annie Bauer, Nancy Mottel, and Howard McLean. From developing engaging class activities such as taste-and-texture labs to volunteering their time with my research projects, these educators went above and beyond to help me succeed, and inspired me to pursue a career in engineering. I am also fortunate to have received superlative advice at a young age about the importance of solving the "big problems" facing our society from my neighbor and friend, Dr. Herbert Bailey, who bartered his insights about mathematics for help with his lawn care.

In addition to taking courses with some of the most innovative engineering educators in the world, Rose-Hulman also fostered a unique culture where

faculty had the time and interest to work on independent research projects. In truth, many of the most valuable lessons from my undergraduate education as an engineer came from these independent research experiences. I am eternally grateful to Dr. Maarij Syed for allowing me to join his research lab during the start of my freshman year at Rose-Hulman. I learned a great deal about the best practices of research, design, and communication during our four years of research. Most importantly, Dr. Syed worked tirelessly behind the scenes by, for example, traveling to campus over breaks so that I could work in the lab and facilitating many unique opportunities for me such as presenting at several international conferences. This foundation has been instrumental to my success in graduate studies. Moreover, I am very appreciative that Dr. Diane Evans took time to discuss probability and statistics when I wandered into her office five years ago. Her boundless enthusiasm for both research and teaching has been a constant source of inspiration toward pursuing a graduate degree. Furthermore, Dr. Daniel Moore, Dr. Marc Herniter, Dr. Ed Doering, and Dr. Robert Throne in the Electrical and Computer Engineering Department and Dr. Roger Lautzenheiser and Dr. Elton Graves from the Mathematics Department always went the extra mile to help me expand my horizons and to challenge me with rigorous end-of-quarter projects during my four years at Rose-Hulman. Moreover, I want to thank Alicia Cross-Engelhardt and Dana Engelhardt for welcoming me to the Urbana-Champaign community. All in all, many people in addition to those listed here, such as the staff at Rose-Hulman or my friends from the community, have also had a significant impact on my pursuit of graduate studies.

Finally, I gratefully acknowledge support for this work in part from the National Science Foundation Graduate Research Fellowship Program under Grant No. DGE - 1144245, the Power Optimization of Electro-Thermal Systems (POETS) National Science Foundation Engineering Research Center with cooperative agreement EEC-1449548, the International Institute for Carbon Neutral Energy Research (WPI-I2CNER), the Office of Naval Research (Grant No. N00014-16-1-2625 with Dr. Mark Spector as the program manager), and the Sandia Academic Alliance with the University of Illinois at Urbana-Champaign with project manager and collaborator Dr. Jason Neely. Sandia National Laboratories is a multi-mission laboratory managed and operated by Sandia Corporation, a wholly owned subsidiary of Lockheed Martin

Corporation, for the U.S. Department of Energy's National Nuclear Security Administration under contract DE-AC04-94AL85000. I2CNER is sponsored by the Japanese Ministry of Education, Culture, Sports, Science and Technology. Finally, electron microscopy measurements of the superhydrophobic samples were carried out in part in the Frederick Seitz Materials Research Laboratory Central Facilities, University of Illinois at Urbana-Champaign.

TABLE OF CONTENTS

LIST OF ABBREVIATIONS

CuO	Copper Oxide
EFE	Electric-Field-Enhanced
FET	Field-Effect Transistor
GaN	Gallium Nitride
HTC	Heat Transfer Coefficient
IR	Infrared
NCGs	Non-Condensable Gases
PCB	Printed Circuit Board
SiC	Silicon Carbide
TLCs	Thermochromic Liquid Crystals

CHAPTER 1

INTRODUCTION

Electrification has catalyzed an increase in the power density (power-to-volume ratio, kW/L) and the specific power (power-to-weight ratio, kW/kg) of both stationary and mobile systems [1, 2, 3, 4, 5, 6]. For stationary systems, electrification has centered around methods for improving the power density, specific power, and efficiency (the ratio of power out to power into a system). Lighter and more compact converters in renewable [3, 7, 8, 9] and high-voltage, high-power grid applications [10, 11, 12] would reduce the installation and maintenance cost of the complete system by decreasing the cost of the support structure and the number of technicians required to perform the installation, which can be a substantial portion of the overall costs. In data centers, more efficient and compact power electronics architectures such as series-stacking [13, 14, 15, 16, 17] can dramatically reduce wasted energy from these growing electrical loads, which currently consume approximately 2% of the energy in the United States of America [18]. For mobile applications, this mega-trend of replacing bulky pneumatic and mechanical systems with smaller electrical systems has catalyzed the development of fully-electric and more-electric: automobiles [1, 19, 20, 21], off-road equipment [22], trains [23, 24, 25, 26], ships [27, 28, 29, 30, 31, 32], and aircraft [33, 34, 35, 36, 37]. Undoubtedly, electrification has created a demand for lighter and more compact power electronics.

Yet, the ability to remove heat from internal hot spots constrains the design of converters and inverters [5, 19, 34, 35, 36, 38, 39, 40, 41, 42, 43, 44, 45, 46, 47]. Depicted in Fig. 1.1, recent advances in the development of high performance power converters utilizing wide bandgap semiconductors have shown that the majority of heat can be generated locally near spatially distributed hot spots [5, 6, 41, 42, 43, 48, 49, 50, 51, 52, 53, 54, 55], especially for application in extreme environments [45, 46, 56, 57, 58]. Traditional cooling schemes are stymied by these spatial as well as temporal variations

in hot spot locations concurrent with electro-thermal optimization and novel circuit architectures [41, 43, 51, 52, 59, 60].

To address this concern, fundamentally different, active cooling techniques are required to mitigate hot spots. Leveraging recent advances both in wide bandgap semiconductors and in phase-change cooling techniques, this work outlines an active hot spot cooling method. Instead of providing uniform single phase or two-phase cooling of the entire device, this thesis builds on the first demonstration of active, phase-change cooling of individual gallium nitride (GaN) transistors using jumping-droplet-based electric-field-enhanced (EFE) condensation as described by the author [63, 64] in order to provide a comprehensive discussion of this promising cooling method for active hot spots in power electronic devices.

Chapter 2 discusses the basic physics governing jumping-droplet condensation and highlights how this yields enhanced heat transfer compared to traditional cooling schemes. Chapters 3 and 4 highlight the potential for external electric [65] and magnetic fields to impact jumping droplets in order to further enhance this heat transfer mechanism. Chapter 5 outlines how to leverage EFE jumping-droplet condensation in a real system to provide both spatial and temporal active cooling for GaN devices. Next, Chapter 6 discusses the construction of the experimental setup developed to investigate this process in ambient conditions. Chapter 7 highlights the model and experimental results developed for the heat transfer analysis of the EFE jumping-droplet condensation for these worst-case conditions of ambient environment with non-condensable gases (NCGs) and jumping against gravity. Evidence of steerable cooling using external electric fields is provided in Chapter 8. Finally, Chapter 9 summarizes the key contributions of this work and future work already in-progress to build on these promising results.

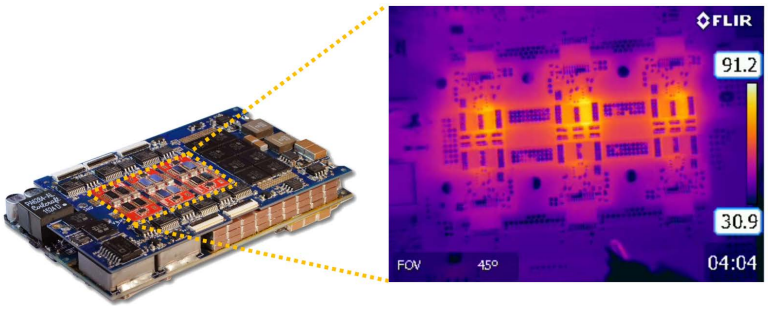

Figure 1.1: High power density inverter with distributed hot spots spatially and temporally based on load [41, 42, 61, 62].

CHAPTER 2

GOVERNING PHYSICAL PRINCIPLES FOR JUMPING-DROPLET HEAT TRANSFER

Water vapor can condense on a surface as either a film or distinct droplets (dropwise) depending on the surface wettability. Simply, wettability describes how well a foreign liquid deposited on either a liquid or solid surface can adhere or spread. This phenomenon is governed by the surface energy (energy per unit area), which can also be viewed as surface tension (force per unit length), at the interface between the surface and the foreign liquid [66]. The affinity for molecules in each material to attract and to interact with similar molecules as opposed to dissimilar molecules causes the area between the two materials to be minimized, which results in surface tension at the interface [66]. When the foreign liquid droplet is at equilibrium with the surface as in Fig. 2.1, three surface tensions or surface energies exist: between the surface and air, γ_{SA}, between the surface and the foreign liquid, γ_{SL}, and the total between the liquid and air, γ_{LA}. As depicted in Fig. 2.1, a contact angle, θ, is formed between the droplet's liquid-air boundary and surface-liquid boundary. This contact angle exists because, unlike bulk liquids, surface molecules do not have neighboring molecules in every direction to provide a balanced net surface tension. Therefore, the lack of surrounding neighboring molecules of similar type creates a net force pulling the molecules inward, which minimizes the surface area for the lowest surface energy state. The surface energy balance in this partial wetting case is

$$\gamma_{SA} = \gamma_{SL} + \gamma_{LA}\cos(\theta). \tag{2.1}$$

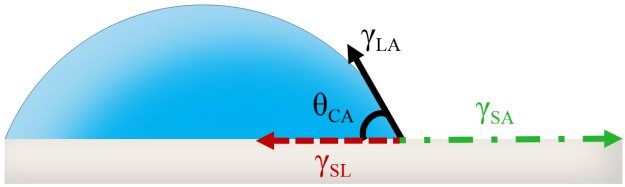

Figure 2.1: Contribution of contact angle to the surface energy balance at equilibrium.

A film or highly pinned droplets would form for complete wetting if $\theta = 0\ ^\circ$ and

$$\gamma_{SA} > \gamma_{SL} + \gamma_{LA}. \tag{2.2}$$

These complete wetting conditions do not promote the jumping phenomenon at the heart of this analysis and will be ignored for the purposes of this discussion. Interestingly, as θ varies between $0\ ^\circ$ and $180\ ^\circ$ for the partial wetting case, a rich diversity of partial wetting behavior exists. This contact angle can either be visualized at the microscale (intrinsic contact angle) or be measured at the macroscale using a microscope (apparent contact angle). Figure 2.2 summarizes how contact angles less than $90\ ^\circ$ yield hydrophilic droplets, which are characterized by a propensity for stronger adhesion to the surface and increased surface energy. In contrast, contact angles greater than $90\ ^\circ$ correspond to hydrophobic droplets that naturally have less attraction to the surface and lower surface energy. As the contact angles diverge further away from $90\ ^\circ$ in both directions, these extreme droplet behavioral states are classified as superhydrophilic for very small contact angles and superhydrophobic for very large contact angles.

Surfaces with the unique superhydrophobic properties can be employed for a wide variety of applications such as anti-fogging [67], anti-icing [67, 68, 69, 70, 71, 72], anti-microbial [73], self-cleaning [67, 71, 73], energy harvesting [74], vapor chambers [75, 76, 77], thermal diodes [78], and enhanced heat transfer [79, 80]. Interestingly, these superhydrophic surfaces also exist in nature. The leaves of lotus plants, the wings of cicadas and butterflies, and

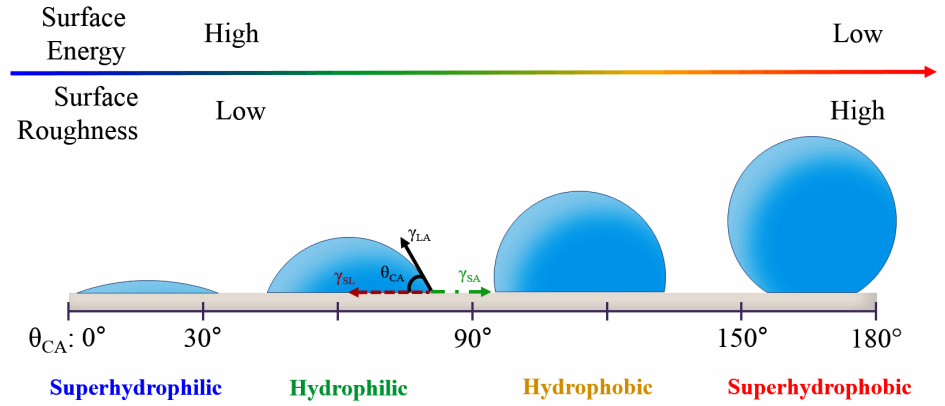

Figure 2.2: Understanding how contact angle yields varying hydrophilic and hydrophobic surface behavior.

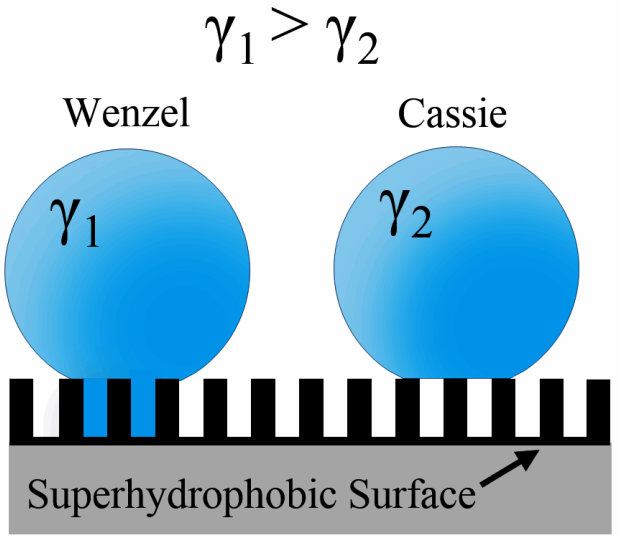

Figure 2.3: Wenzel-like droplet morphology has stronger adhesion to surface than Cassie-like droplet morphology.

the feet of geckos and water striders all exhibit hydrophobic and superhydrophobic properties [66, 81, 82].

Since the high surface roughness of superhydrophobic nanostructures facilitates the formation of droplets with lower surface energy as shown in Fig. 2.2, this surface behavior type is ideal for catalyzing droplet jumping. The surface energy of a droplet is also governed by its morphology for droplet formation and this can dramatically impact a droplet's capacity to jump. In general, the droplets will exhibit either Wenzel-like morphology, where a portion of the droplets flow into the valleys of the nanostructured surface, or Cassie-like morphology where the droplets sit on top of the nanostructured surface. As shown in Fig. 2.3, droplets with the Cassie-like morphology clearly have less adhesion to the surface and therefore less surface energy than droplets with Wenzel-like morphology even in cases where the surface roughness is the same [66]. Thus, developing surfaces that promote the Cassie-like morphology will be important to catalyzing the jumping behavior because the droplets will have inherently lower surface energy [66, 76, 83, 84].

This jumping phenomenon exists when neighboring droplets merge (coalescence) on a superhydrophobic surface composed of nanostructures with high surface roughness [75, 76, 85, 86]. Figure 2.4 demonstrates how the merging of two identical droplets with the same contact angle, θ_{CA1}, radius, R_1, and

contact line radius, r_1, results in a droplet where the volume is conserved:

$$V_n = 2V_1 = 2\left(\frac{4}{3}r_1^3\right), \tag{2.3}$$

and the contact angle remains the same:

$$\theta_{CAn} = \theta_{CA1}. \tag{2.4}$$

Yet, as the droplets squeeze into each other in order to maintain the same contact angle and contact line radius with the new volume, the surface energy of the merged droplet ends up being less than the sum of the surface energy for each individual un-merged droplet as in Fig. 2.4. Since energy must be conserved, some excess energy exists in the merged state compared to the initial un-merged state. As a result of forces created internally to the droplet from the squeezing during coalescence, this excess energy is spontaneously converted into kinetic energy, which catalyzes the droplet to eject normal to the surface (independent of gravity) as in Fig. 2.5. This jumping behavior, described by the energy balance equation of the surface energies and the kinetic energy of the merged droplet (K_3):

$$\gamma_1 + \gamma_2 = \gamma_3 + K_3, \tag{2.5}$$

exists also when the droplets are of differing size as depicted in Fig. 2.5 [76, 86]. The surface energy is based on the surface tension, σ, and the

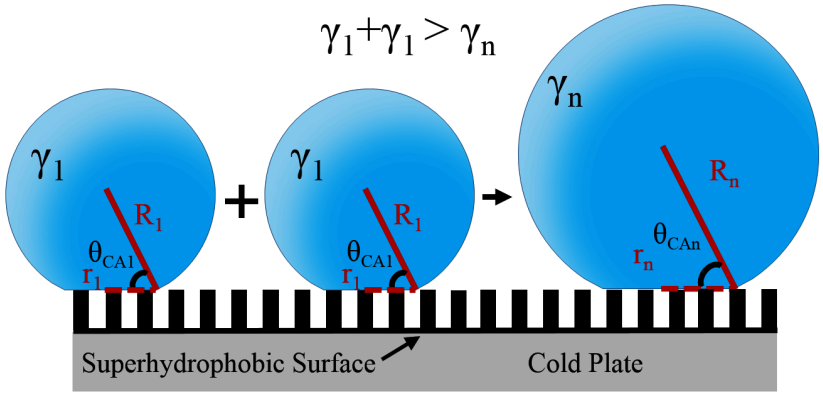

Figure 2.4: Ideally, when two identical droplets merge, volume should be conserved and the resulting contact angle should remain the same.

surface area of the merged droplet:

$$\gamma_3 = \sigma\left(4\pi R_3^2\right), \tag{2.6}$$

while the kinetic energy is based on the density of the liquid (ρ), the volume, and the velocity (U_f) of the merged droplet:

$$K_3 = \left(\frac{1}{2}\rho\right)\left(\frac{4}{3}\pi R_3^3\right)\left(U_f\right). \tag{2.7}$$

The velocity of the jumping droplet can be determined from

$$U_f = C\sqrt{\frac{6\sigma(r_1^2 + r_2^2 - (r_1^3 - r_2^3)^{2/3})}{\rho(r_1^3 + r_2^3)}}. \tag{2.8}$$

Interestingly, this jumping behavior exists even though less than 6% of the initial energy of the un-merged state is often converted into kinetic energy during the merged state [76, 83, 84, 85]. The nanostructured surfaces are fabricated specifically to promote the formation of droplets with diameters between approximately 1 and 100 μm since droplets of this scale are best suited to have excess surface energy after merging with a neighboring droplet and to jump [75, 76, 85]. Moreover, these surfaces are also designed to promote the Cassie-like morphology to further reduce the surface energy and to promote jumping.

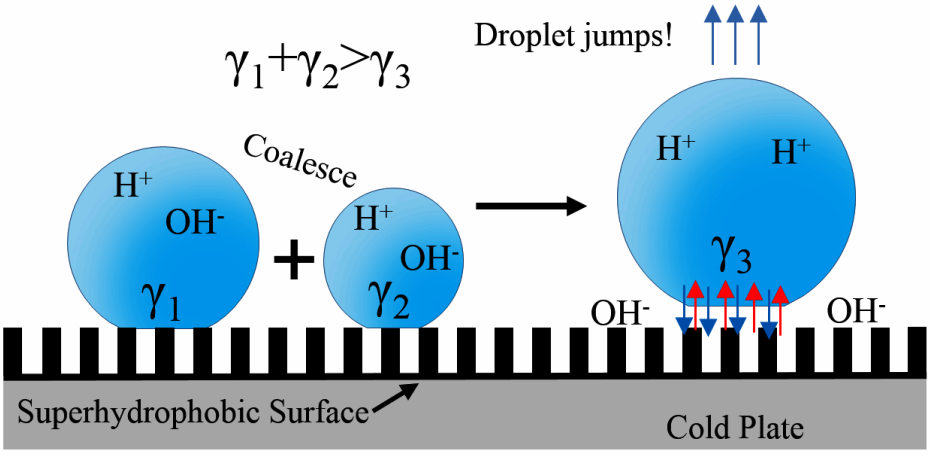

Figure 2.5: Once two droplets merge on the superdyrdophobic surface, they jump independent from gravity due to excess surface energy. The droplet also has a net positive charge.

Dropwise condensation is significantly more efficient at heat and mass transfer since the droplets can more easily shed from the surface via jumping or even gravitational body force compared to adhered liquid films [85]. Additional improvements to this heat transfer can be obtained both if the droplets jump off the surface (independent of gravity) instead of rolling off the surface due to gravity [87] and if the droplets undergo phase change from liquid to gas (evaporation). Furthermore, jumping-droplet condensation can enhance heat transfer in two different ways. First, the jumping behavior decreases the time-averaged droplet size residing on a condensing surface such as a cold plate or pipe, which increases the condensation rate and can increase the condensation heat transfer coefficient by several orders of magnitude [76, 83]. Second, jumping also catalyzes cooling when the droplets are attracted to a surface using latent heat while evaporating. This provides a new parallel heat transfer path from the hot to cold surface with an ultra-high evaporation heat transfer coefficient.

Interestingly, Fig. 2.5 also demonstrates another unique aspect of the jumping phenomenon where the droplet has a net positive charge after leaving the surface. Chapter 3 examines how external electric fields impact the droplet trajectory due to this net charge.

CHAPTER 3

ELECTRIC-FIELD-ENHANCED JUMPING

While external factors such as the roughness of the superhydrophic coating, gravity, and the presence of NCGs impact the jumping process, external electric fields have been shown to impact droplet trajectory, and thus, can maximize the efficiency of jumping-droplet cooling. Jumping droplets were recently found to have a net positive charge of approximately 10 to 100 fC [65, 76, 87]. As the droplets leave the superhydrophobic surface as shown in Fig. 2.5, a small amount of OH^- remains on the nanostructured surface due to electric double layer charge separation, which yields excess H^+ in the water droplet. Figure 3.1a demonstrates how jumping droplets show no special attraction to the electrode when no potential difference exists between the electrode and a cold plate. Yet, when the electrode is negatively charged with respect to the cold plate, Fig. 3.1b highlights how the trajectories of the droplets immediately trend towards the negatively charged electrode. In contrast, droplets are strongly repelled by the electrode if a positive potential is applied between the electrode and cold plate.

Thus, by replacing the electrode with an electronic device such as a GaN transistor, external electric fields could be employed to guide jumping droplets

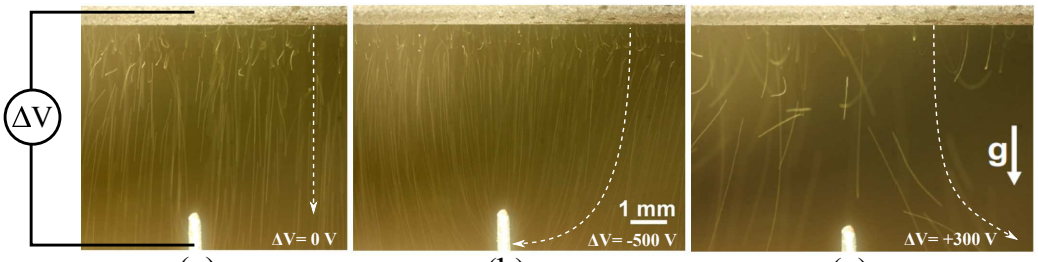

Figure 3.1: For an exposure time of 40 ms, measurements with (a) 0 V, (b) -500 V, and (c) +300 V between an electrode and a cold plate underscored that jumping droplets in an electric field are attracted to a negative potential and repelled by a positive potential [65, 76, 87].

toward the hot electronic components. A review of the fundamentals for electric fields will ensure that the corresponding voltages and distances for EFE jumping-droplet condensation will be practical for electronics cooling. Consider an experimental setup where droplets will condense and jump from a cold plate toward a hot GaN transistor, which will be outlined with more detail in Chapters 5 and 6. For varying spacing and applied voltage between the cold plate and GaN device for this experimental setup, the magnitude of the electric field (V/m) between the cold plate and the negatively biased GaN device can be calculated from

$$E = \frac{V}{d}, \tag{3.1}$$

where V is the bias voltage (e.g. -100 V) and d is the separation between the cold plate and the GaN device (e.g. 3 mm). The force (N) due to the electric field acting on the charged jumping droplet (e.g. $q \approx 15$ fC) can be obtained from

$$F = qE. \tag{3.2}$$

All in all, the magnitude of this force due to the electric field was calculated for varying bias voltages and separation distances as depicted in Fig. 3.2. For a large bias voltage of -100 V, the magnitude of the force is 1.5 $\times 10^{-9}$ N for a separation of 1 mm and 5 $\times 10^{-10}$ N for a separation of 3 mm. As the bias voltage was reduced to -1 V, the smallest force calculated was still 5 $\times$ 10^{-12} N. This force is greater than the force due to gravity on these droplets [65, 76, 87]. Thus, external electric fields have a significant impact on droplet trajectory and have the capacity to enhance the efficiency of heat transfer due to jumping-droplet condensation for power electronics applications.

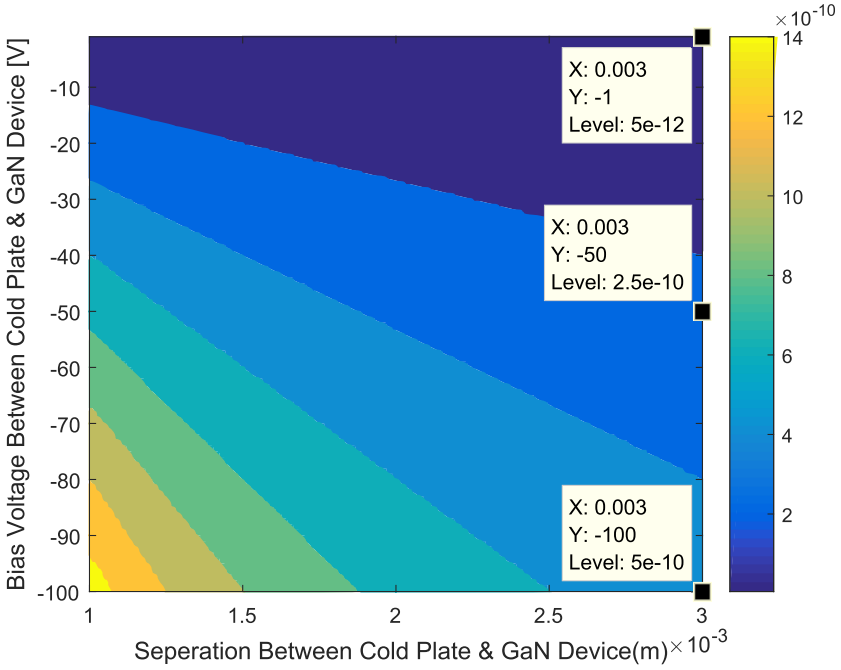

Figure 3.2: Magnitude of the force due to the electric field on the charged jumping droplet (color scale) for varying bias voltages and distances between the droplet and the GaN device.

CHAPTER 4

IMPACT OF MAGNETIC FIELDS ON JUMPING DROPLETS

Since electric fields were shown to have a significant impact of jumping droplet trajectory, will magnetic fields have a similar impact? To address this question, a review of magnetic fields from first principles is valuable. Simply, a moving charge generates a magnetic field. The cylindrical coordinate system is convenient for solving problems involving magnetic fields because the conservation of magnetic flux ensures that magnetic flux lines must form complete loops. Fig. 4.1a provides an overview of the cylindrical coordinate system. For problems with symmetry, Ampere's law simplifies the magnetic field calculations as compared to the Biot-Savart law. Ampere's law can be employed by drawing an Amperian loop around the infinite line of current as shown in Fig. 4.1b. The current passes through the Amperian loop along the z-axis and generates a magnetic field with the direction found by the right hand rule. The differential length of the Amperian loop in cylin-

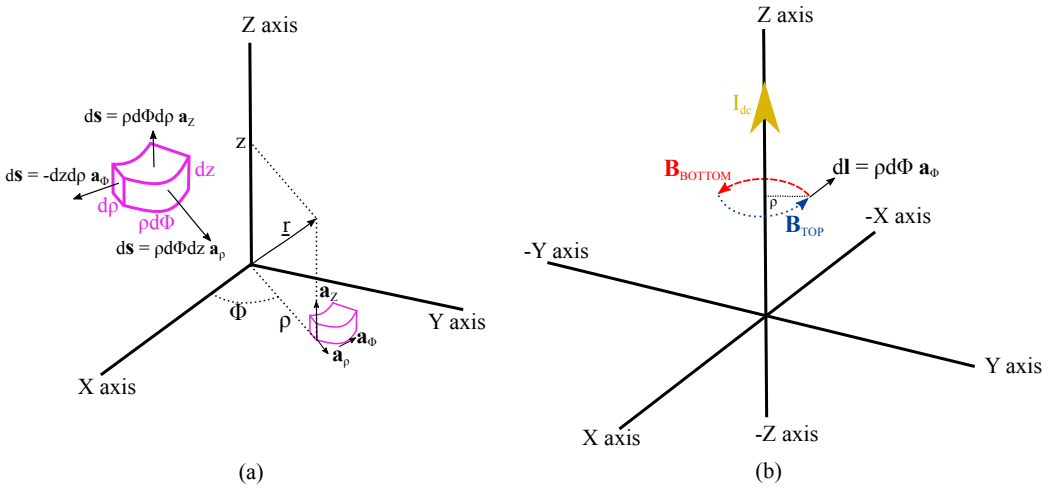

Figure 4.1: (a) Review of cylindrical coordinates and (b) Amperian loop for infinite line of current.

drical coordinates as shown in Fig. 4.1b is

$$d\mathbf{l} = \rho d\phi \mathbf{a}_\phi. \tag{4.1}$$

The magnetic field clearly depends on ρ, the distance from the line of current [m], and can be expressed formally. For this discussion, vector quantities have bold typeface and scalar variables have regular typeface. From Ampere's law, the magnetic field along the closed Amperian loop is equal to the current enclosed by the loop as in

$$\oint \mathbf{H} \cdot d\mathbf{l} = \quad I_{enc} \tag{4.2}$$

$$\oint \left(H\mathbf{a}_\phi\right) \cdot \left(\rho d\phi \mathbf{a}_\phi\right) = \quad I_{enc} \tag{4.3}$$

$$\rho H \oint_{\phi=0}^{\phi=2\pi} d\phi = \quad I_{enc} \tag{4.4}$$

$$2\pi\rho H = \quad I_{enc}. \tag{4.5}$$

Recalling that the magnetic field is in the $\mathbf{a}_\phi$ direction, the magnetic field vector, $\mathbf{H}$ [A/m], for this symmetric current flow is

$$\mathbf{H} = \frac{I_{enc}}{2\pi\rho}\mathbf{a}_\phi. \tag{4.6}$$

The actual magnetic field for the jumping-droplets circuit board, which is discussed in detail in Section 6.2, is slightly more complicated than this fundamental example as depicted in Fig. 4.2, but this assumption for symmetry and ideal conditions will provide an upper bound for this initial "order of magnitude" analysis for the impact of magnetic fields on jumping droplets. Next, the magnetic flux density can be found by multiplying the result for the magnetic field by the permeability of the material through which the field is flowing. In this case, the material is free space, so the permeability is $\mu_o = 4\pi \times 10^{-7}$ H/m. Thus, the magnetic flux density, $\mathbf{B}$ [T], can be

calculated from

$$\mathbf{B} = \mu_o \mathbf{H} \tag{4.7}$$

$$\mathbf{B} = \frac{\mu_o I_{enc}}{2\pi\rho}\mathbf{a}_\phi. \tag{4.8}$$

As shown in Fig. 4.3, the magnetic flux density falls off quickly with distance. This is an important observation because the magnetic flux density will determine how much magnetic fields will impact the trajectory of a jumping droplet. In other words, the magnetic flux density is directly proportional to the force exerted on the charged droplet. Prior research has shown that jumping droplets have a positive charge of approximately 15 fC [65, 76, 87]. From the magnetic portion of the Lorentz force law, the force, $\mathbf{F}_B$ [N], on this moving jumping-droplet charge by the magnetic field from the current in the circuit can be found:

$$\mathbf{F}_B = q\mathbf{v} \times \mathbf{B}. \tag{4.9}$$

Recalling that the cross product depends on the sine of the angle between the vectors, the maximum force will exist when the droplet's trajectory (velocity vector) is perpendicular to the magnetic flux density vector. If this case alone is assumed, an upper limit on the Lorentz force can be obtained for various droplet velocities and external magnetic flux densities. From

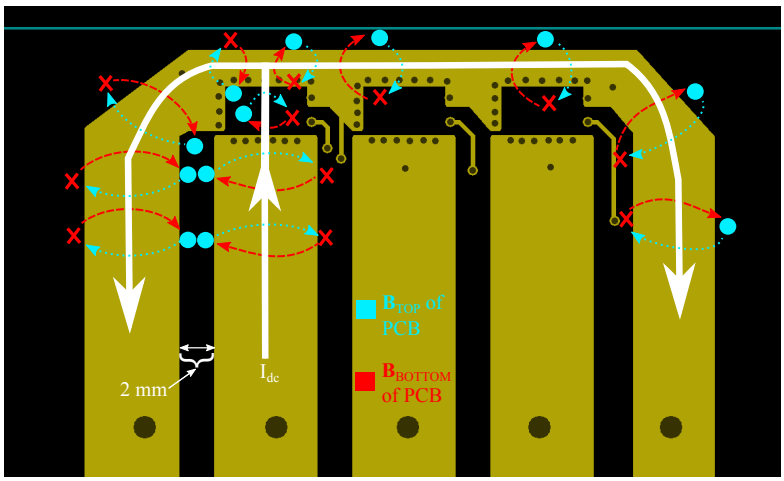

Figure 4.2: Artistic rendering of magnetic fields generated by dc current flow in jumping droplets PCB described in Chapter 6 and Appendix A.

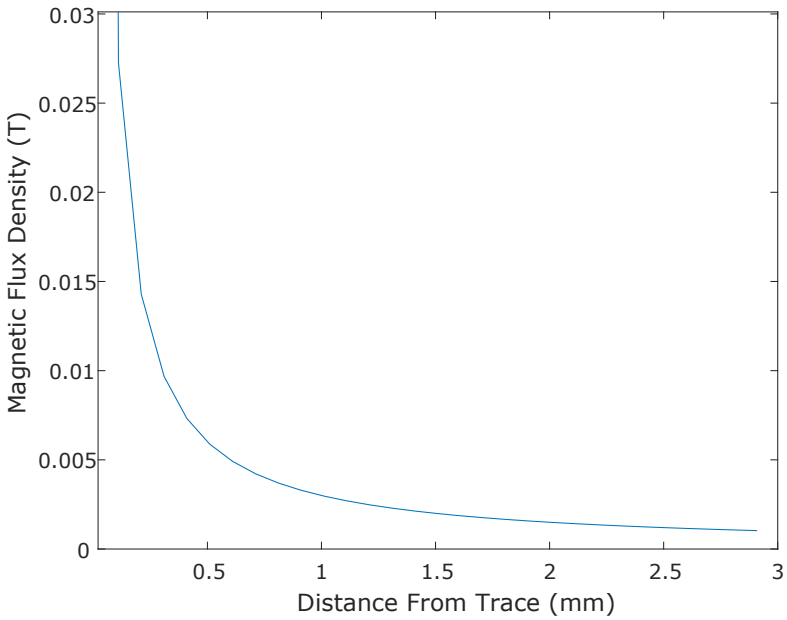

Figure 4.3: How magnetic flux density from the 15 A dc current in the circuit board change with distance.

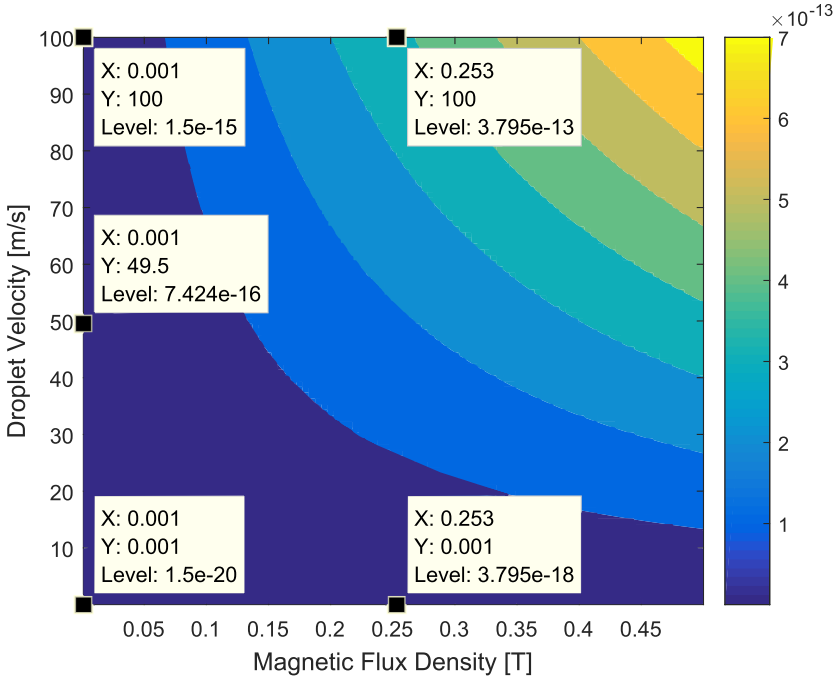

Figure 4.4: Magnetic portion of the Lorentz force (color scale) based on changing droplet velocity and external magnetic flux density.

Fig. 4.4, the maximum force estimated for a droplet 3 mm away from the GaN device (B = 1 mT) was 1.5 $\times 10^{-20}$ N for a droplet velocity of 1 mm/s and 1.5 $\times 10^{-15}$ N for a droplet velocity of 100 m/s. If the same two droplet

velocities are considered when the droplet spacing from the GaN FET is only 10 μm (B = 0.2 T, which is a very large magnetic field), the magnetic Lorentz force is still only 3.5 $\times 10^{-18}$ N and 3.5 $\times 10^{-13}$ N respectively.

As the bias voltage in the electric field study of Chapter 3 was reduced to -1 V, the smallest force calculated was still 5 $\times 10^{-12}$ N, which is orders of magnitude greater than the 1.5 $\times 10^{-15}$ N magnetic Lorentz force seen at this same distance even for a high velocity of 100 m/s. This analysis has shown that the magnetic Lorentz force is several orders of magnitude smaller than the force due to an electric field. This agrees with intuition since the magnetic flux densities and droplet velocities in this experiment are small. For the magnetic Lorentz force to be significant, the droplet velocity and the external magnetic field would need to be very large as shown in Fig. 4.5. Since these ranges for external magnetic field and droplet velocity are not physically possible for the proposed experiment, the impact of the magnetic field on the trajectory of jumping droplets can be neglected without loss of generality.

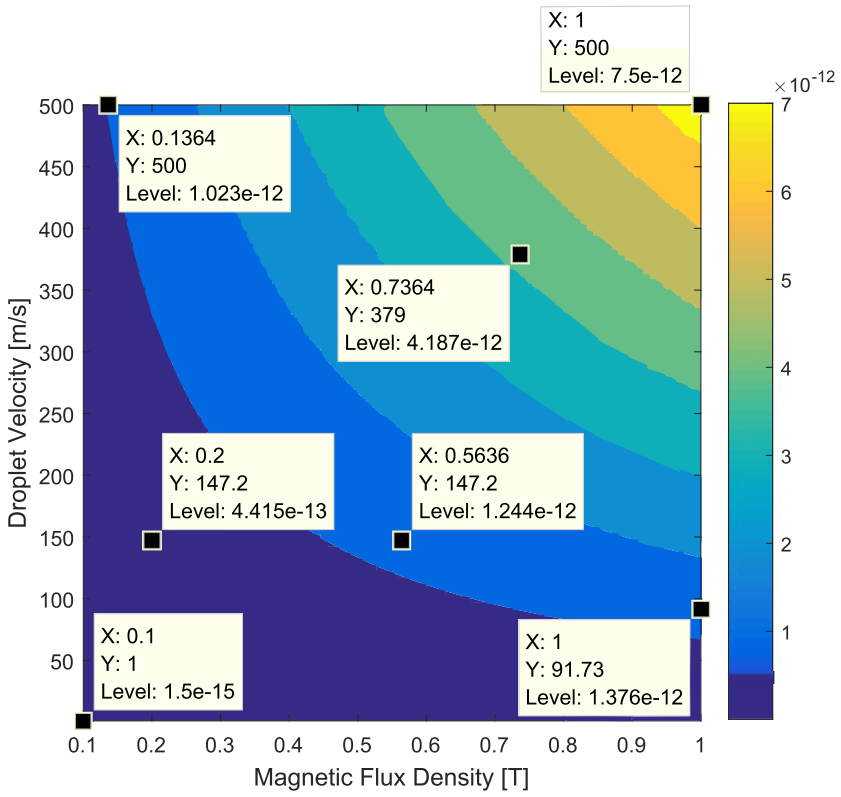

Figure 4.5: Large magnetic fields and droplet velocities are needed for the magnetic portion of the Lorentz force (color scale) to be significant.

CHAPTER 5

PROPOSED ACTIVE COOLING METHOD

Wide bandgap transistors incorporating GaN and silicon carbide (SiC) are catalyzing the development of higher power density and higher efficiency converters by providing lower parasitics, such as on-state resistance, package inductance, and output capacitance, and smaller physical package size. Yet, as the package size decreases and the power processed remains the same (and possibly increases), the surface area to cool the device dramatically decreases and the capacity to extract heat with conventional methods becomes very difficult and ultimately constrains improvements in power density and specific power of the complete system due to the necessity of a large heat sink. Figure 5.1a provides an example infrared (IR) thermal photo of a hot spot for a compact GaN transistor shown in Fig. 5.1b. The integration of an advanced cooling technique with chip-scale wide bandgap transistor packages would improve reliability and device performance by maintaining lower device junction temperatures.

Methods for incorporating phase-change materials into heat sinks for power electronics have focused primarily on hybrid heat sinks with metal foams [90] and alkane isomers such as n-eicosane [91, 92]. Similarly, liquid to gas phase-change refrigerant materials have been employed as a passive means to cool downhole electronics for drilling applications [93, 94]. This transition (i.e. solid to liquid or liquid to gas) acted as a passive cooling mechanism to mitigate heat from the high peak power transients of low duty-cycle pulsed power supplies for applications such as aircraft landing gear or downhole drills [93, 94, 95]. While phase-change heat transfer is commonly applied to low duty-cycle power electronics converters like aircraft landing gear using waxes that transition from solid to liquid [90], few commercial power electronics systems utilize closed-loop evaporation and condensation-based phase-change cooling techniques. Thus, jumping-droplet condensation is an appealing mechanism to investigate for liquid-to-gas phase-change cooling of

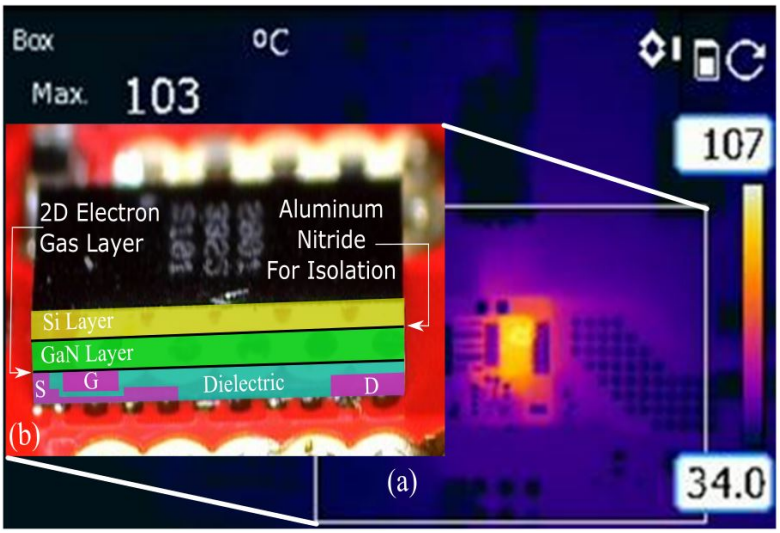

Figure 5.1: (a) Thermal photo of GaN with conduction losses from 15 A of dc current and (b) structure of EPC2034 GaN transistor [88, 89].

high power density electronics. Moreover, since modern power converters have hot spots that vary spatially and temporally, traditional passive techniques are not sufficient and pose a major obstacle to increasing the power density and specific power of the system. Therefore, enabling active cooling with EFE jumping droplets would truly be disruptive if both spatial and temporal active cooling can be demonstrated.

In contrast, this work proposes the development of an active cooling method for power electronics. Figure 5.2 illustrates two possible realizations of this heat transfer method where external electric fields enable active, steerable cooling of hot spots inside of a power electronics package. In both cases, this setup comprises a vapor chamber containing a colder surface connected to a larger heat sink or a cooling loop and a hotter surface connected to the hot spots within the power electronic device. While GaN transistors have been selected to represent generic power electronics hot spot generators for these examples and experiments, these hot spot generating devices could be any passive (i.e. inductor, capacitor), active (i.e. transistor, diode, etc.), or support logic (e.g. gate driver, digital isolator, microcontroller, etc.) component. In the realization of Fig. 5.2a, the vapor chamber serves as a high-heat-flux heat spreader or heat sink in order to route heat away from the small form factor GaN transistor [75, 76]. The vapor chamber would need to be joined to the GaN devices with the lowest possible thermal impedance

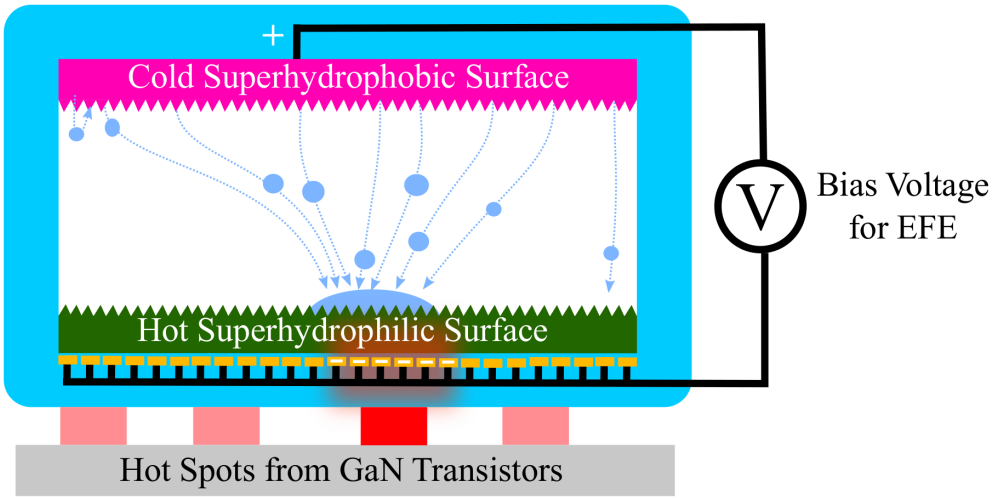

(a) Heat sink or heat spreader on top of hot spots

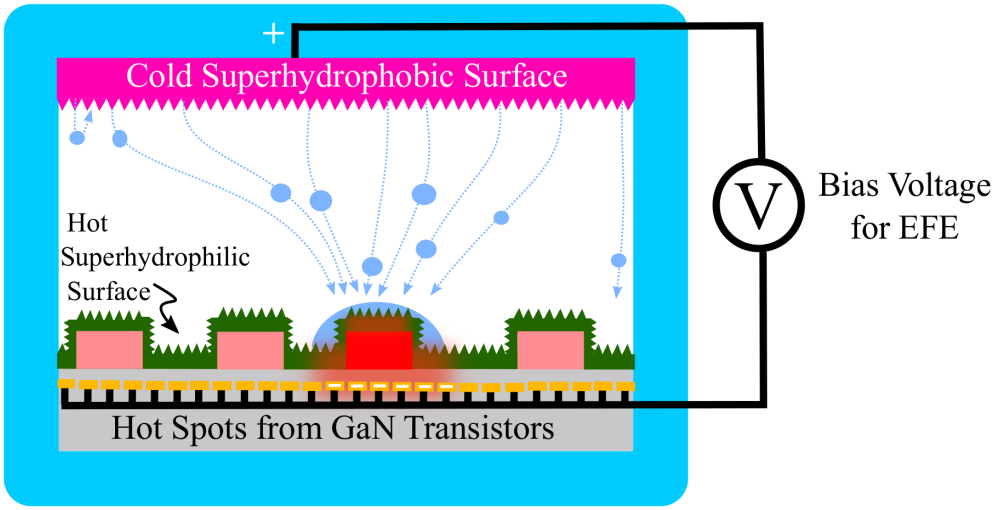

(b) Heat sink or heat spreader enclosing hot spots

Figure 5.2: Employing external electric fields in a vapor chamber for active cooling with jumping droplets either as an external heat spreader or heat sink [75, 76] for the hot spot or (b) enclosing the hot spot.

(e.g. soldered, etc.) since this series thermal impedance would ultimately be the limiting factor for extracting heat from the GaN transistor. Moreover, the GaN devices could also be placed within the vapor chamber in order to avoid the series thermal impedance of the contact mechanism proposed in the first realization altogether. Depicted in Fig. 5.2b, this scheme would require the superhydrophilic coating or an additional thin layer to provide

electrical isolation between other components within the chamber.

Using the realization of Fig. 5.2a as an example, Fig. 5.3 summarizes the four constantly repeating steps of the heat transfer cycle within the vapor chamber. To facilitate droplet jumping inside of the vapor chamber, a superhydrophobic coating is deposited on the colder surface so that the vapor stored at a low pressure within the chamber will condense on this surface as in Fig. 5.3a. When the droplets jump from cold surface, external electric fields can either be turned on actively or passively in order to steer the droplets toward the hot spots with EFE jumping as in Fig. 5.3b. EFE also

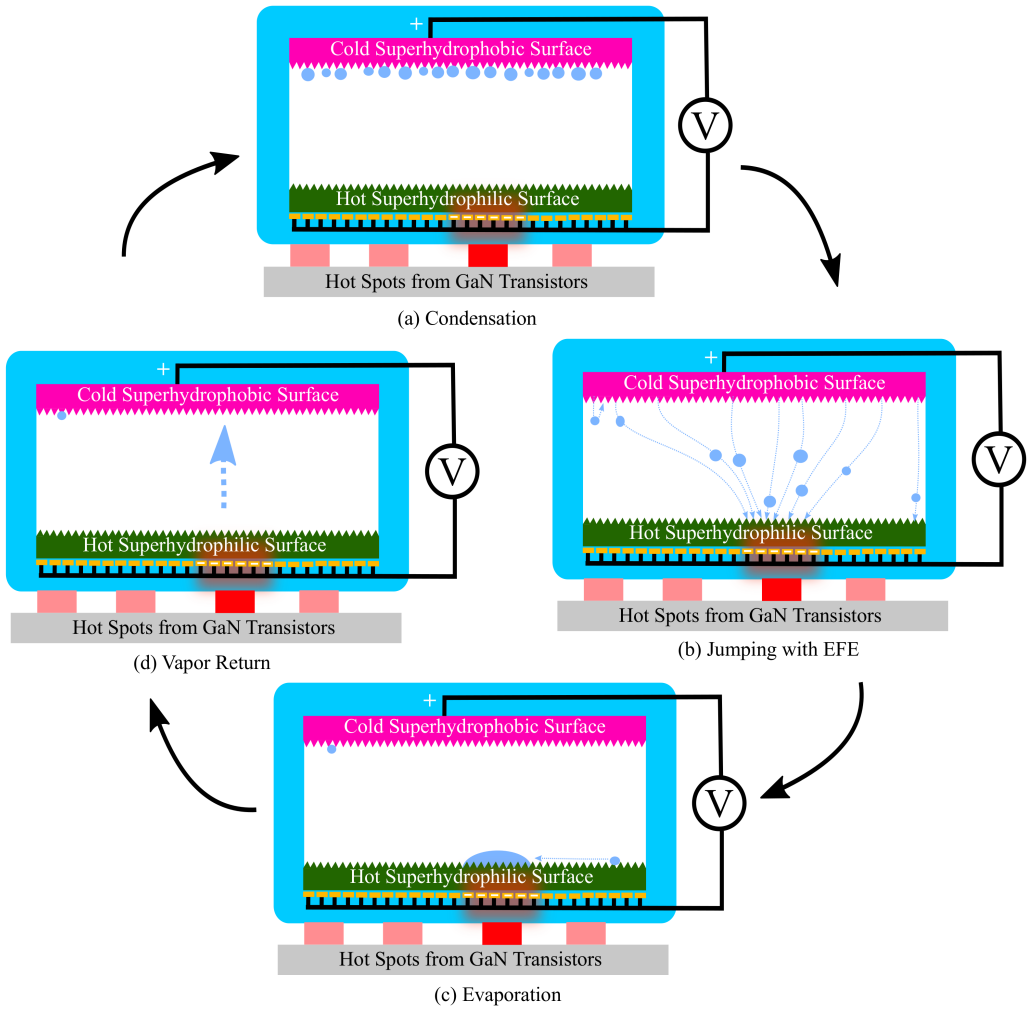

Figure 5.3: Overview of jumping-droplet heat transfer cycle with (a) droplets condensing on cold superhydrophobic surface, (b) jumping and following electric field lines to hot superhydrophilic surface, (c) droplets evaporate when the hit the hot surface or wick toward hot spot, and (d) vapor returns through the chamber cavity to the cold surface so that the cycle can continue.

increases the percentage of droplets that reach the hot side instead of immediately returning back to the cold surface after jumping. One way to realize active control would involve decisions from a microcontroller about which portions of the hot side to bias with external electric fields in order steer the droplets appropriately. This type of control could be determined based on feedback from temperature measurements, or *a priori* knowledge of the gate signals or the mission profile of the hot spot device would allow cooling to be coordinated with the activation of this device (e.g turn-on and turn-off of a GaN transistor). In contrast, the parasitic capacitances and large dv/dt transitions within switching power supplies could also potentially be harnessed as a means for generating these external electric fields. Once the droplets reach the hot side, a superhydrophilic coating can be integrated in order to enable droplets that did not reach the hot spots to wick toward the hot spots as in Fig. 5.3c. When cold droplets evaporate off the hot surface, they extract tremendous heat. As shown in Fig. 5.3d, this heat is transferred through the open chamber to the cold side as vapor due to latent heat. When this vapor reaches the cold superhydrophobic surface, the heat is transferred into the surface as the vapor condenses back into droplets. In summary, this proposed active cooling approach can enable a disruptive improvement in heat transfer because it is closed-loop, has the capacity for active cooling of hot spots via external electric fields, and does not require capillary paths to transfer the vapor back to the cold side for condensation like those in heat pipes.

For this study, the cooling scheme depicted in Fig. 5.2b was selected so that the jumping behavior and heat transfer with and without EFE could be examined. Chapter 6 describes the design and development of this experimental testbed. Instead of immediately analyzing this phenomenon at low pressure, these experiments were implemented in the ambient environment where the natural atmosphere served as the vapor chamber boundaries and medium.

CHAPTER 6

JUMPING-DROPLET CONDENSATION EXPERIMENTAL TESTBED

6.1 Overview of Experimental Setup

To investigate jumping-droplet electronics cooling, a printed circuit board (PCB) with multiple integrated GaN field-effect transistors (FET, EPC2034) was positioned above a nanostructured superhydrophobic CuO surface as in Figs. 6.1 and 6.2. The PCB with the hot transistors was placed above the cold CuO sample in order to test the worst case scenario of droplet jumping against gravity. The droplet condensation and jumping behavior were examined during the experiments with a high resolution PhantomCinemagII video camera with a Canon macro lens. Section 6.2 provides rationale for the

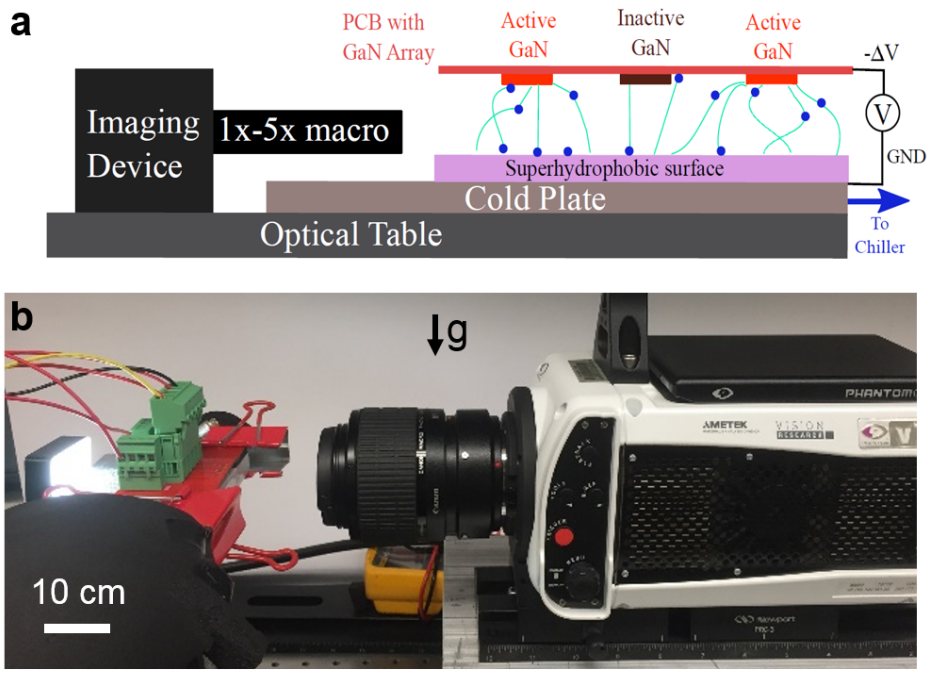

Figure 6.1: (a) Side view schematic and (b) photograph of the experimental setup for characterizing jumping-droplet cooling of GaN transistors.

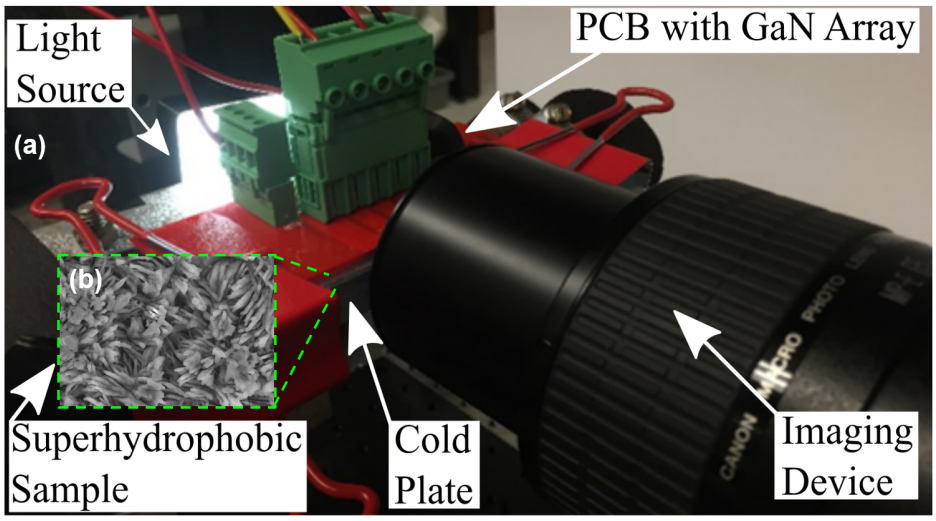

Figure 6.2: (a) Critical aspects of experimental hardware. (b) Scanning electron micrograph of a C_4F_8 functionalized ($\approx$ 50 nm) superhydrophobic CuO surface.

design of the circuit and the PCB layout for this testbed. The sample fabrication process employed to develop the superhydrophobic samples depicted in Fig. 6.2b is described in Section 6.4 [83, 96, 75, 76, 97].

6.2 Design and Layout of PCB

The structure of the chip-scale EPC2034 enhancement mode GaN-on-silicon power MOSFET shown in Fig. 5.1b does not have a large surface area for cooling and has been designed with a smaller thermal impedance from the junction to the top surface compared to the thermal impedance from the junction to the bottom of the device [88, 89]. Thus, this device was incorporated into the circuit of Fig. 6.3 in order to evaluate the proposed cooling technique with and without contribution of external electric fields. The electric field could be developed by electrically floating either the source pins of the transistor or the ring of copper placed around the power devices to a negative potential. Three EPC2034 GaN transistors were placed in parallel as shown in Fig. 6.4. The GaN devices were placed 3 mm apart on the circuit board so that, as shown in Figs. 6.1 and 6.2, they could be captured within the same frame of the high-resolution PhantomCinemagII video camera. Kelvin connections to measure the voltage directly across the drain

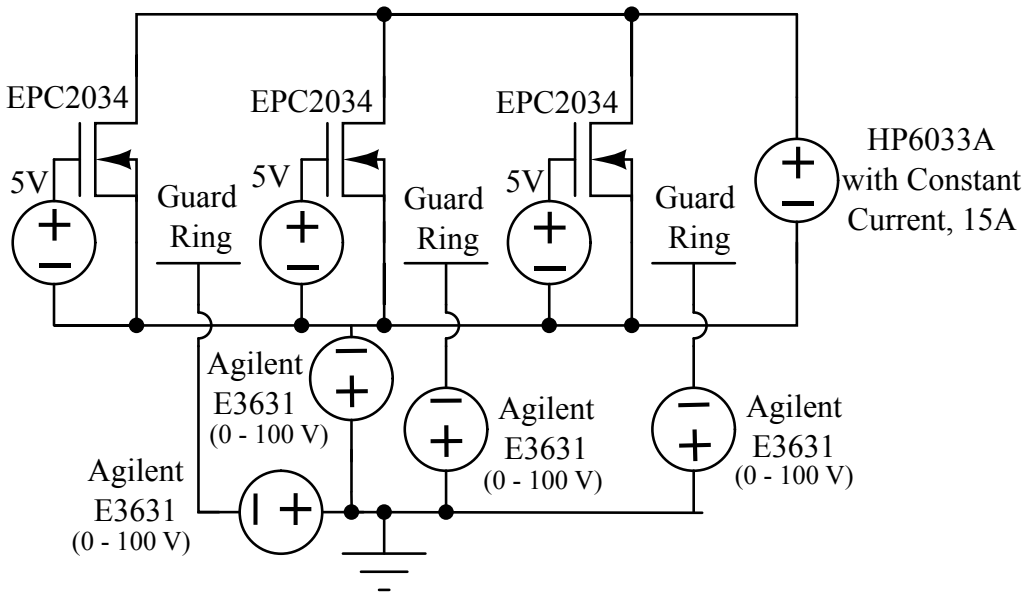

Figure 6.3: Schematic for PCB to probe proposed cooling method.

and source pins of each GaN device were also included so that the power dissipated by each transistor could be measured with high precision. Additionally, the gate connection for each GaN device was routed to a connector so that this could be controlled externally. Since rubber spacers with specific thicknesses (1 mm to 5 mm) were used to ensure uniform spacing between the GaN transistors and the cold superhydrophobic sample, 30 mm of empty space was intentionally designed at the left and right edge of the PCB so that PCB could sit directly on top of these rubber spacers. Metal binder clips, which sandwiched the rubber spacers between the PCB and cold plate together, also ensured that the experimental setup did not move during testing as in Fig. 6.2a.

As a first step, the conduction losses for various currents were evaluated. As shown in Fig. 5.1a, the GaN FET quickly becomes a hot spot with 15 A of dc current flowing. Since experimental evidence with the first revision of the PCB revealed that electrically floating the source pins of the transistor was more effective at steering the droplets as discussed in Chapter 8, a second revision of the circuit was developed to provide complete isolation between two GaN devices as shown in the schematic of Fig. 6.5 and the hardware photograph of Fig. 6.6. Schematics and PCB artwork created on KiCad EDA for both generations of this testbed can be found in Appendix A.

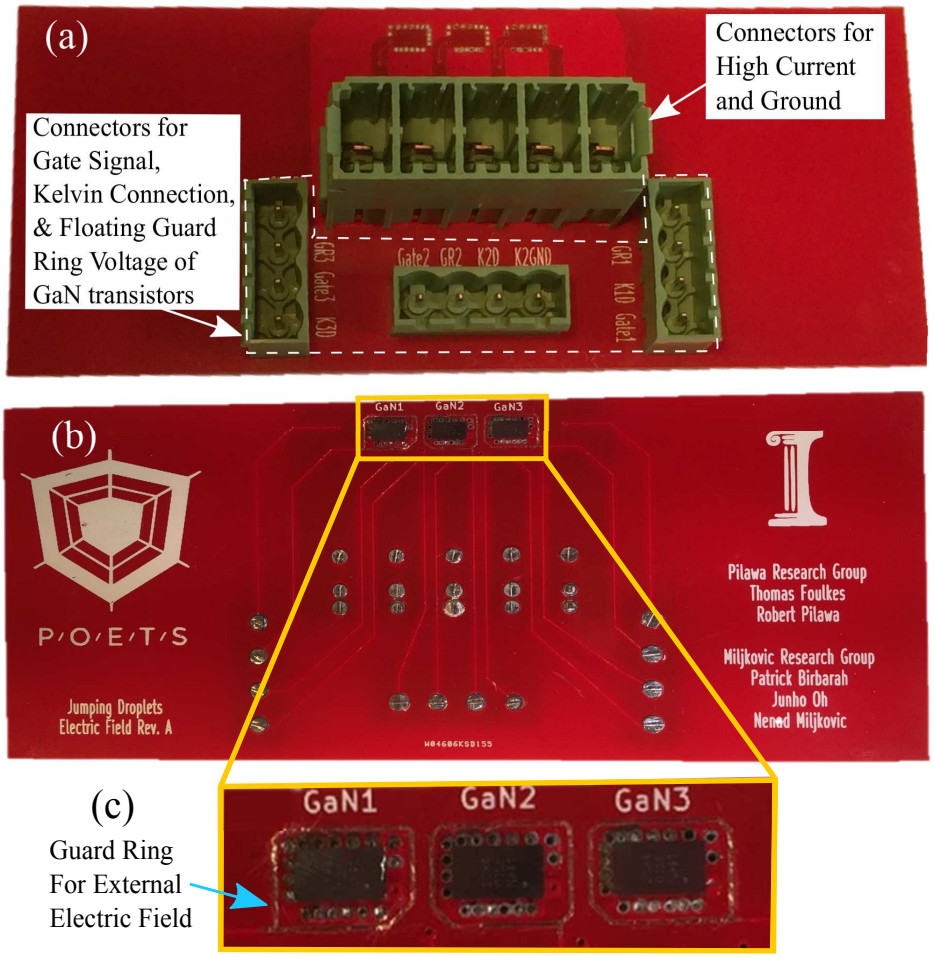

Figure 6.4: (a) Back and (b) front of a PCB developed to probe cooling with and without external electric fields by electrically floating either (c) a guard ring around the EPC2034 devices or the source pin of the devices.

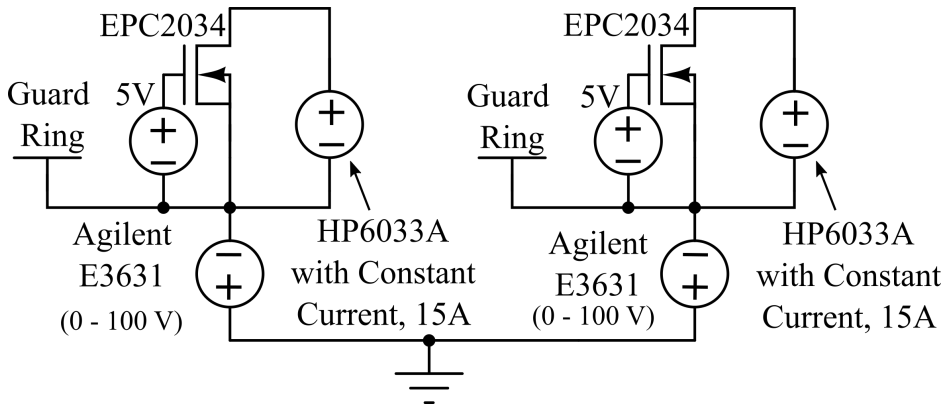

Figure 6.5: Schematic for revision 2 of the testbed containing GaN tranistors with complete electrical isolation.

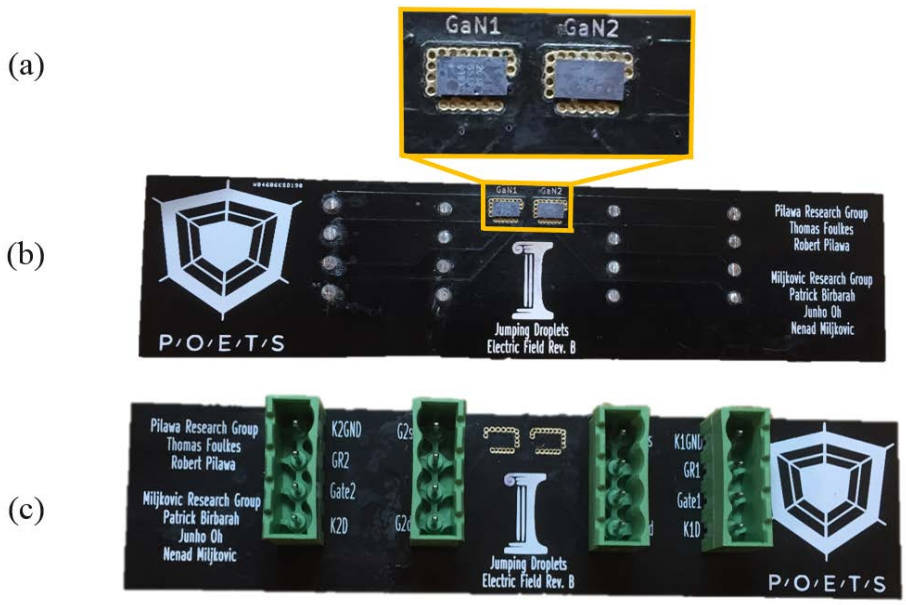

Figure 6.6: Heat transfer enhancement with and without external electric fields can be examined by electrically floating either (a) a guard ring around the EPC2034 devices or the source pin of the devices located on the (b) front of a PCB. The GaN devices are electrically isolated. Connections to the testbed can be made to connectors on the (c) back of the PCB.

6.3 Measuring Temperatures and Controlling Power Supplies

Yet, the inability to view the device while integrated with the superhydrophobic surface required the use of thermocouples. By attaching thermocouples to the transistor and the cold plate, quantification of the GaN FET steady-state temperature for various spacings (1 mm to 5 mm) between the circuit and cold superhydrophobic sample was studied. The thermocouple measurements were acquired using a National Instruments USB X Series Multifunction DAQ. Through USB-to-GPIB, the same LabVIEW program could update the voltage and current settings of the Agilent E3631 and HP6033A power supplies in real-time. More information about data acquisition and control of the experimental setup can be found in Appendix B.

6.4 Preparation of the Superhydrophobic Sample

The CuO nanostructures of Fig. 6.2 were grown on commercially purchased 800 m thick Cu tabs with overall length and width dimensions of 50 mm by 50 mm. Figure 6.7 summarizes the five steps of the sample cleaning and fabrication process. First, each Cu tab was cleaned in an ultrasonic bath with acetone for 10 minutes and rinsed with ethanol, isopropyl alcohol, and deionized (DI) water. The tabs were then dipped into a 2.0 M hydrochloric acid solution for 10 minutes to remove the native oxide film on the surface, then triple rinsed with DI water and dried with clean nitrogen gas. Nanostructured CuO films were formed by immersing one of the cleaned tabs into a hot ($\approx$ 98 °C) alkaline solution composed of $NaClO_2$, NaOH, $Na_3PO_4{\cdot}12H_2O$, and DI water (3.75: 5: 10: 100 wt. %) [75, 76, 83, 96, 97]. During the oxidation process, a thin ($\approx$ 300 nm) Cu_2O layer was formed that then re-oxidized to form sharp, knife-like CuO oxide structures with heights of h $\approx$ 1 m, a solid fraction of $\phi \approx 0.02$ and a roughness factor of r $\approx$ 10. To render the CuO tabs superhydrophobic, a C_4F_8 hydrophobic coating was applied with chemical vapor deposition. This process allowed for the development of a highly conformal polymer layer on the CuO surface ($\approx$ 50 nm thick). Goniometric measurements, also known as contact angle measurements, using a MCA-3 Kyowa Interface Science microscope of $\approx$ 300 nL droplets on a smooth C_4F_8-coated silicon wafer surface showed advancing and receding contact angles of $\theta_a = 121 \pm 5.1$ ° and $\theta_r = 105 \pm 9$ °, respectively. Meanwhile, the apparent advancing and receding contact angles on the superhydrophobic CuO surface were measured to be $\theta_a^{app} = 166 \pm 6$ ° and $\theta_r^{app} = 156 \pm 7$ °, respectively. Step 5 of Fig. 6.7 depicts an example measurement of these apparent advancing and receding contact angles for the CuO nanostructured superhydrophobic samples.

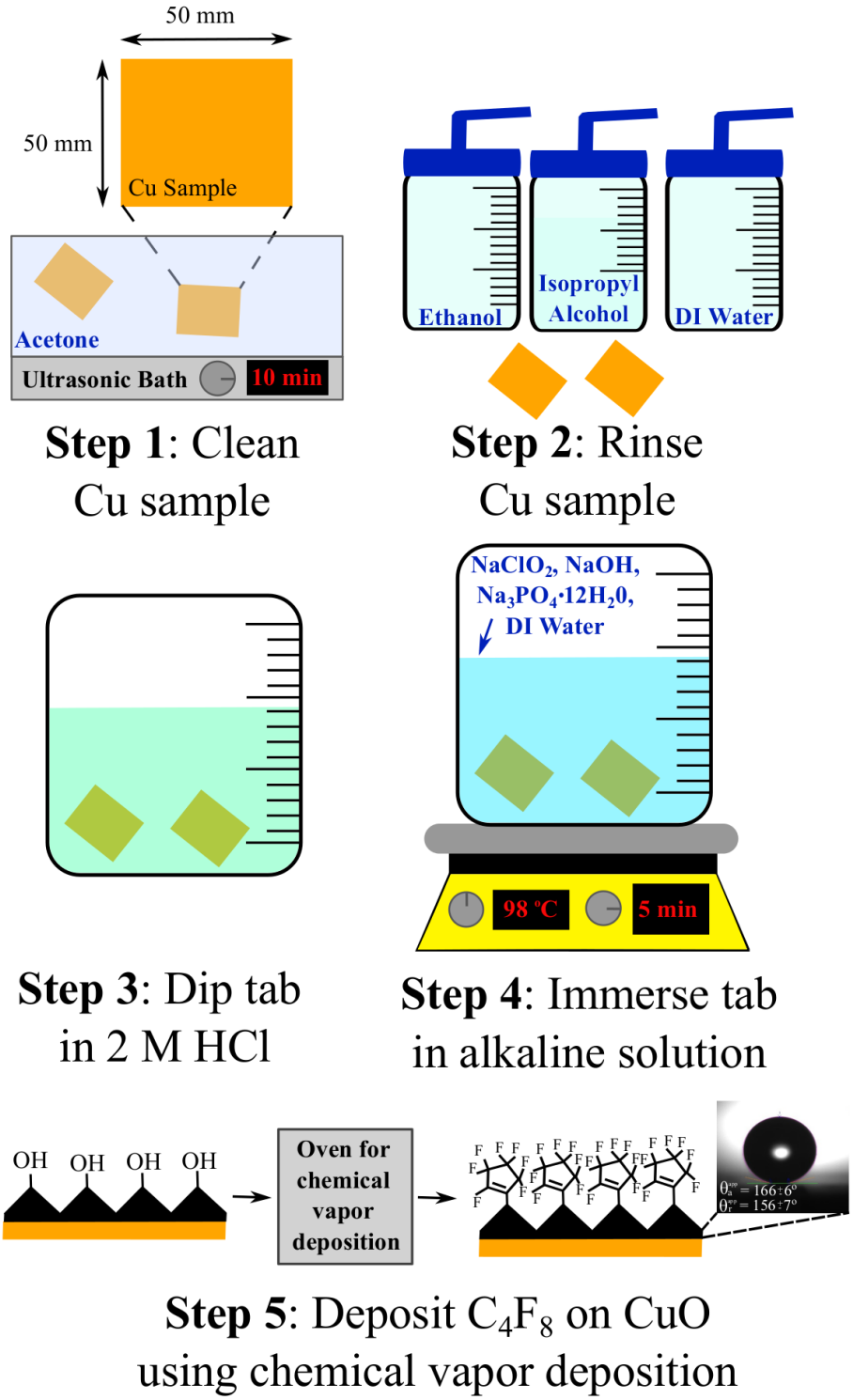

Figure 6.7: Fabrication of CuO surfaces with superhydrophobic behavior from C_4F_8 nanostructures.

CHAPTER 7

HEAT TRANSFER IN AMBIENT CONDITIONS

7.1 Overview of Proposed Thermal Resistance Network

The thermal resistance of the network for this experimental setup is depicted in Fig. 7.1. This thermal network simplifies the calculation of the heat transfer breakdown for the system. The GaN device was assumed to have a uniform temperature, T_g, due to the low Biot number (Bi $\approx 10^{-2}$) for the cooling conditions and geometry studied here. By attaching thermocouples to

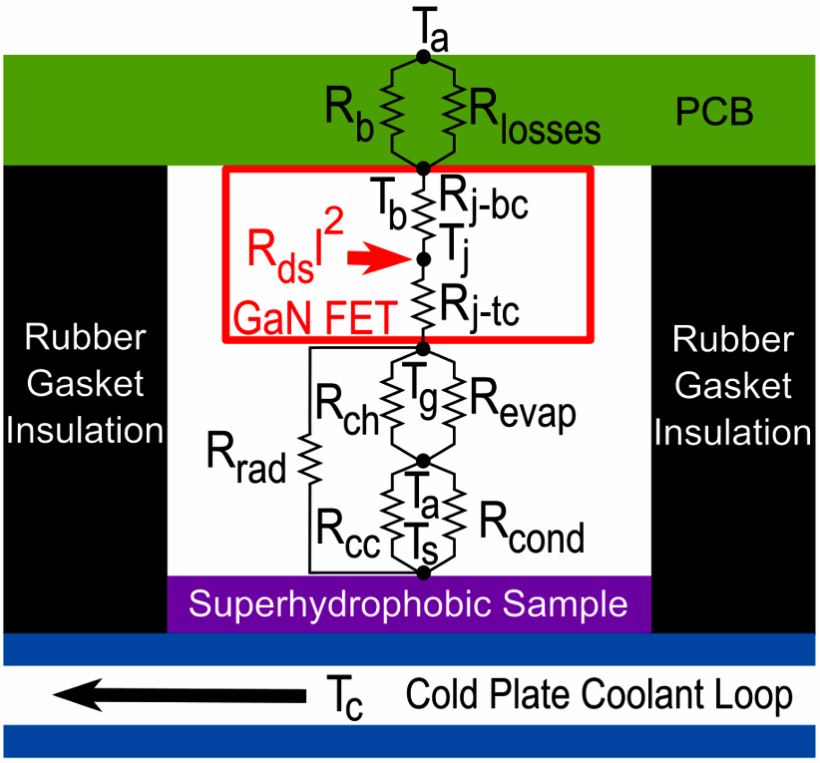

Figure 7.1: Thermal resistance network for experimental setup.

the transistor and the cold plate, an examination of the transistor's steady-state temperature for various spacings of the GaN transistor and the cold superhydrophobic sample was implemented. For 15 A of dc current flowing through an on-state resistance of 7 mΩ (corresponding to the manufacturer measurement of on-state resistance at 25 °C [88, 89]), 1.57 W of Joule heating, Q_g, for the GaN was observed. Using

$$\Psi_g = \frac{Q_g}{A_g}, \tag{7.1}$$

this heat was combined with the cross-sectional area for this EPC2034 GaN FET to generate a heat flux of 13.2 W/cm^2. Assuming that the rubber gaskets offer ideal insulation, the cooling benefit can be separated into its contributing factors of radiation, convection, conduction through the back of the PCB to the ambient air of $T_a = 23 \pm 0.5$ ^{o}C, and heat removed by evaporation via jumping droplet condensation from the cold superhydrophobic surface, $T_s = 5 \pm 0.5$ ^{o}C. Miscellaneous losses to ambient air have been lumped into a thermal resistance, R_{losses}, and were determined through calibration during the no-jumping condition.

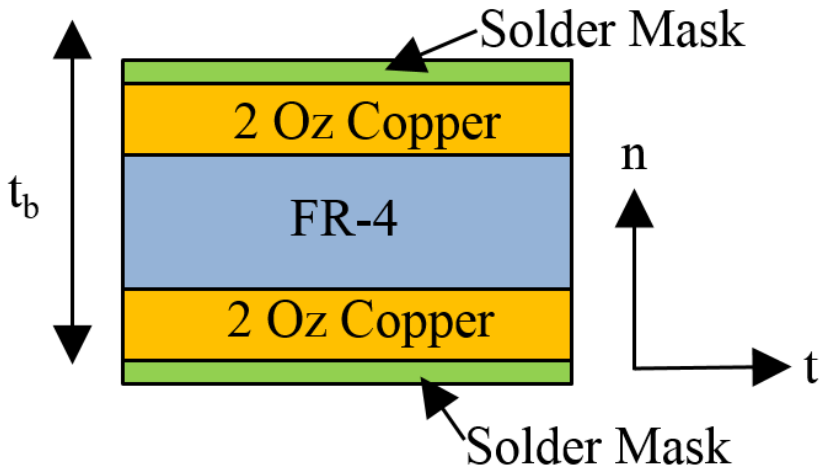

Figure 7.2: Composition of PCB with normal (n) and tangential (t) directions shown relative to the thickness, t_b. Layer thicknesses are not to scale.

7.2 Modeling Spreading Resistance in PCB

The thermal impedance for the back of the PCB, R_B, involves spreading resistance within the PCB and convection to air with convection heat transfer coefficient (HTC) to ambient, h_{nat}. As a first step toward developing a model for the spreading resistance, the thermal conductivity of the PCB, k_b, must be determined. This spreading resistance is composed of tangential and normal components as depicted in Fig. 7.2. The tangential thermal conductivity, $k_{b,t}$, through the length of the PCB composed of FR-4 and copper was found using

$$k_{b,t} = \frac{k_f t_f + k_c t_c}{t_f + t_c}, \tag{7.2}$$

where the material parameters and thicknesses are summarized in Table 7.1. To simplify this expression, t_c represents the combined thickness of both 2 Oz copper layers in the PCB. The contributions of the solder mask layers were neglected for these heat transfer approximations since the thickness and thermal conductivity for these layers are negligible compared to those of FR-4 and 2 Oz copper. Using the parameters from Table 7.1, the thermal conductivity of the PCB in the normal direction as indicated by Fig. 7.2 was obtained from

$$k_{b,n} = \Big(\frac{t_f}{t_f + t_c}\frac{1}{k_f} + \frac{t_c}{t_f + t_c}\frac{1}{k_c}\Big)^{-1}. \tag{7.3}$$

Last, the tangential and normal thermal conductivities can be combined in a weighted sum to find the PCB's total thermal conductivity, k_b, as in

$$k_b = \Big(\frac{t_b}{w_b}\Big)k_{b,t} + \Big(1 - \frac{t_b}{w_b}\Big)k_{b,n}, \tag{7.4}$$

which was recorded in Table 7.1.

Since the PCB is significantly wider than it is thick, the normal component of the spreading thermal conductivity has dramatically more weight and represents the main path for heat flow. PCB vias near the GaN FETs were included to increase heat transfer in this normal component direction. Observations using an infrared camera in the laboratory also support this modeling assumption. The spreading of heat from the source into the PCB was modeled using an ellipsoid geometry with axes of t_b, w_b, and r_g. The

Table 7.1: Dimensions and Material Parameters for Experimental Setup

Parameter	**Definition**	**Values**	**Units**
A_s	area of the superhydrophobic sample	6.25	cm^2
A_g	cross-sectional area of GaN FET	0.12	cm^2
A_b	area of entire PCB	16.29	cm^2
w_b	width of the PCB	5.2	cm
w_g	width of GaN FET	2.6	mm
l_g	length of GaN FET	4.6	mm
r_g	radius for GaN FET	1.8	mm
t_f	thickness of FR-4	302.5	μm
t_c	combined thickness of both 2 Oz copper layers	140	μm
t_b	thickness of the PCB	1.6	mm
k_f	thermal conductivity of FR-4	0.2 to 0.3	W/mK
k_c	thermal conductivity of 2 Oz copper	355 to 390	W/mK
k_b	thermal conductivity of PCB	33.6 to 36.1	W/mK
h_{nat}	convection HTC to ambient	1 to 10	W/m^2K

radius for GaN FET modeled as a circular source is

$$r_g = \left[(w_g l_g)/(\pi)\right]^{-1/2}. \tag{7.5}$$

Including the contribution of the thermal impedance of convection to air, the thermal resistance through the back of the PCB would be the sum of the spreading resistance and the resistance of natural convection on the PCB:

$$R_B = \frac{1}{\pi k_b r_g} \tan^{-1}\left(\frac{t_b + w_b}{r_g} - \frac{\pi}{4}\right) + \frac{1}{h_{nat} A_b} \tag{7.6}$$

where coefficients and board parameters are summarized in Table 7.1.

7.3 Validating Spreading Resistance Model

Two different schemes were employed to verify independently both the model for the spreading resistance in the PCB and the thermocouple temperature measurements of the GaN devices and the PCB. First, an infrared (IR) camera can provide a map of heat spreading such as Fig. 7.3a corresponding to the conduction losses of 15 A of dc current through the GaN transistor, but not absolute temperature measurements because the emissivity of the PCB and components are difficult to determine. For this experiment, a piece of opaque Kapton was placed on the PCB to provide a reference emissivity of approximately 0.95 to calibrate the IR measurement. In contrast, thermochromic liquid crystals (TLCs) are a tool to observe the absolute temperature of the PCB and the components. TLCs reflect visible light in response to temperature. The time delayed images of Fig. 7.4a track how the heat map changes as the system approaches thermal steady state for a continuous drain current of 15 A in each transistor from startup. Thermal steady-state was reached at 30 seconds. The TLCs from LCR Hallcrest (Product Number: SPN100R70C20W) used in this study had an activation temperature of 70 °C and a bandwidth of 20 °C. The PCB and components were coated first with black paint before applying the TLCs such that all reflected light would correspond to a continuous mapping of color to temperature from 70 °C (red) to 90 °C (violet). Both the black paint and the TLCs were applied uniformly using an airbrush.

Specifically, the images corresponding to t = 10 seconds and t = 30 seconds highlight the validity of the assumption that the spreading resistance follows a three-dimensional ellipsoid. Thus, the measurement obtained with the TLCs supplements the IR and the thermocouple measurements with an independent probe of the system's heat map during thermal steady state.

7.4 Thermal Paths from Junction to Case of GaN Device

Heat generated based on Eq. 7.1 dissipates from the GaN transistor's junction to the top and bottom of the package following the thermal resistance network of Figs. 7.1 and 7.3b. For the EPC2034 GaN device utilized in this study, the thermal resistances from the junction both to the case top, R_{j-tc}, and to the case bottom, R_{j-bc}, are summarized in Table 7.2 [88, 89]. These high performance devices favor top-side cooling since R_{j-tc} is slightly more than a tenth the size of R_{j-bc}.

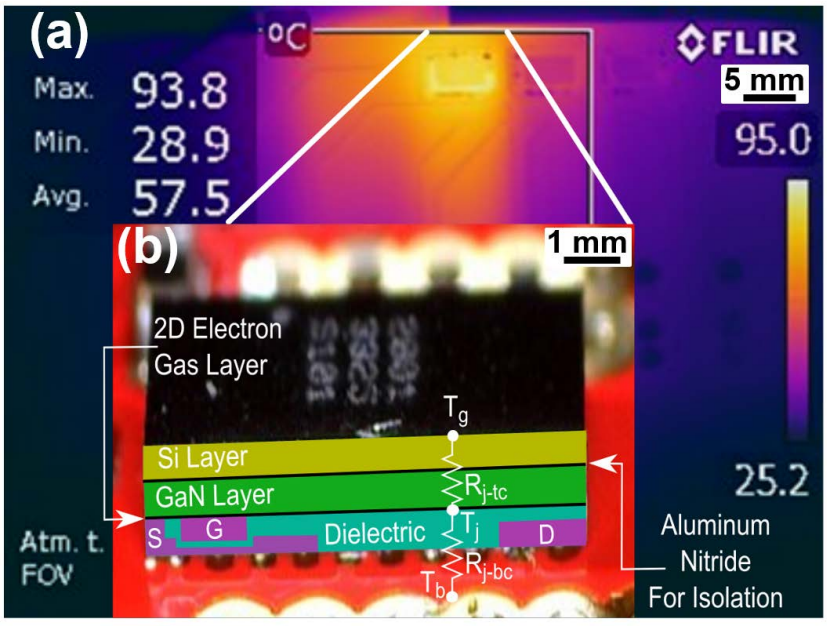

Figure 7.3: (a) IR thermal photo of a GaN device with the (b) thermal impedance network from the junction.

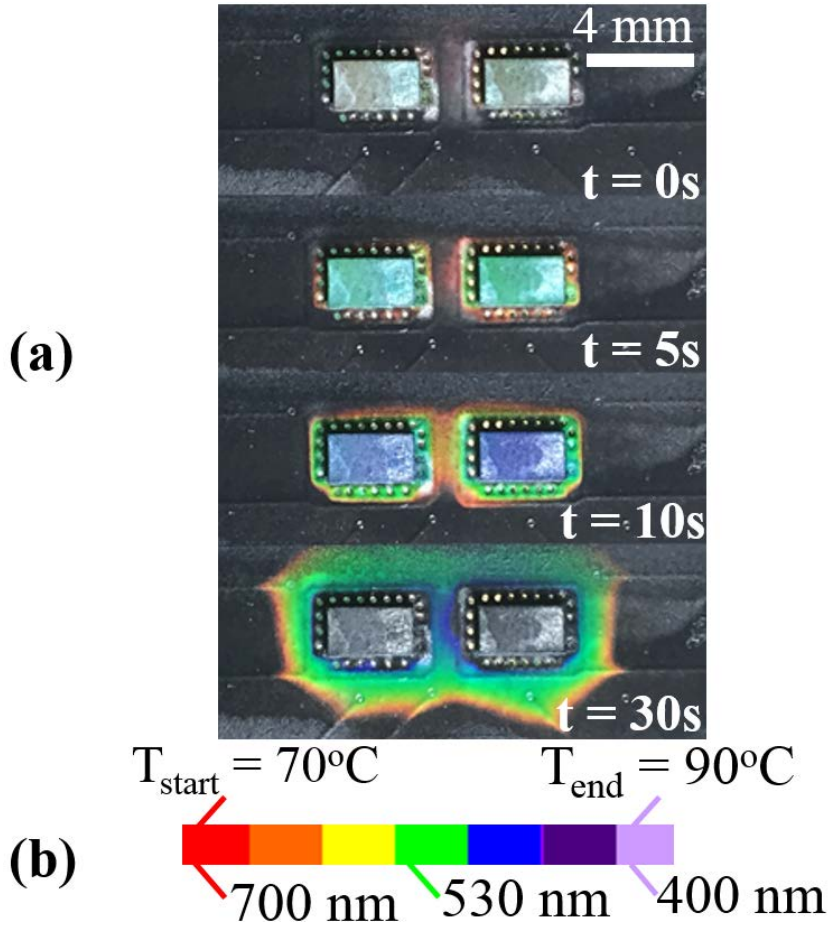

Figure 7.4: (a) Composite time-lapse liquid crystal thermochromic images of the two GaN devices during startup where the (b) visible color map translates to temperature.

Table 7.2: Thermal Resistances for EPC2034 Device [88, 89]

Parameter	**Definition**	**Value**	**Units**
R_{j-tc}	junction to case top	0.45	K/W
R_{j-bc}	junction to case top	3.9	K/W

7.5 Thermal Impedances Between GaN FET and Superhydrophobic Sample

Next, the thermal impedance between the GaN transistor and the cold superhydrophobic sample can be subdivided into five parts with experimental setup dimensions and material parameters described in Table 7.1 and the HTCs for these front side thermal network components summarized in Table 7.3. First, the natural convection from the hot GaN device, R_{ch}, can be captured by a thermal resistance of

$$R_{ch} = \frac{1}{h_{ch} A_g}. \tag{7.7}$$

Similarly, the natural convection from the cold superhydrophobic sample, R_{cc}, has a thermal resistance equivalent to

$$R_{cc} = \frac{1}{h_{cc} A_s}. \tag{7.8}$$

Table 7.3: Heat Transfer Coefficients and Material Parameters for Calculations

Parameter	**Definition**	**Values**	**Units**
A_s	area of the superhydrophobic sample	6.25	cm^2
h_{ch}	convection HTC on hot surface	1 to 10	W/m^2K
h_{cc}	convection HTC on cold surface	1 to 10	W/m^2K
h_{nat}	convection HTC to ambient	2 to 5	W/m^2K
h_{cond}	condensation HTC for ambient	100 to 1,000	W/m^2K
h_{rad}	radiation HTC	5 to 9	W/m^2K
h_{evap}	evaporation HTC due to jumping droplets	parameter under test	W/m^2K

The condensation on the superhydrophobic sample, R_{cond}, can be modeled by a thermal resistance of

$$R_{cond} = \frac{1}{h_{cond} A_s}. \tag{7.9}$$

Based on the Stephan-Boltzmann's constant, the GaN device temperature, T_g, and the superhydrophobic sample temperature, T_s, the HTC for radiation can be found

$$h_r = 5.67 * 10^{-8}(T_g^2 + T_s^2)(T_g + T_s). \tag{7.10}$$

Thus, the radiation thermal resistance from the hot GaN FET to the cold superhydrophobic sample is

$$R_{rad} = \frac{1}{h_{rad} A_g}. \tag{7.11}$$

While h_{evap} is one of the main parameters under test, the thermal impedance associated with evaporation from the GaN transistor is

$$R_{evap} = \frac{1}{h_{evap} A_g}. \tag{7.12}$$

All in all, the equivalent thermal impedance for the network on the front side of the PCB corresponds to

$$R_F = \left[\left(\frac{1}{h_{ch} A_g} || \frac{1}{h_{evap} A_g} \right) + \left(\frac{1}{h_{cc} A_s} || \frac{1}{h_{cond} A_s} \right) \right] || \frac{1}{h_{rad} A_s}. \tag{7.13}$$

where coefficients and board parameters are summarized in Table 7.1 and $||$ represents a parallel impedance operation required to obtain the correct result. The temperatures in the thermal network of Fig. 7.1 are the measured GaN FET device temperature, T_g, the measured superhydrophobic sample temperature, T_s, and the approximate temperature of the ambient 25 °C laboratory, T_a.

7.6 Determining Miscellaneous Losses of Model Based on Experimental Measurements

Based on measurements of current passing through and voltages across the GaN transistor under test, the heat generated by the GaN device, Q_g, for each experimental condition can be determined. Similarly, experimental measurements of the package temperature and the superhydrophobic sample temperature were also obtained for each case. These measurements are summarized in Table 7.4. Based on these measurements, updated calculations and refined ranges for several of the HTC are also provided in Table 7.4.

Table 7.4: Refining Parameter Definitions Based on Experimental Measurements and Calculations

Parameter [Units]	**No Jumping**	**Jumping**	**EFE Jumping**
Q_g [W]	1.6 ± 0.4	1.6 ± 0.4	1.6 ± 0.4
T_g [°C]	90 ± 1	88 ± 1	87 ± 1
T_s [°C]	5 ± 0.5	5 ± 0.5	5 ± 0.5
A_g [cm^2]	0.12 ± 0.01	0.12 ± 0.01	0.12 ± 0.01
h_{nat} [W/m^{2}K]	2 to 5	2 to 5	2 to 5
h_{cond} [W/m^{2}K]	100 to 1,000	100 to 1,000	100 to 1,000
h_{rad} [W/m^{2}K]	7.60	7.52	7.48

Employing Eqs. 7.2 through 7.13, the thermal resistances introduced in Fig. 7.1 were calculated and recorded in Table 7.5. These thermal impedances will serve as the foundation of a quantitative model to determine the miscellaneous thermal losses, which form a resistance in parallel with the thermal resistance through the back of the PCB to ambient, R_B. An estimate of these miscellaneous losses must be obtained before the HTC associated with the evaporation due to jumping-droplet condensation can be calculated.

Experimentally, without jumping droplets ($h_{evap} = 0$), the temperature of the GaN device was measured to be $T_g = 90 \pm 1$ °C. Based on Fig. 7.5, the intersection of various R_{losses} curves and $h_{evap} = 0$ corresponds to the curve with $R_{losses} = 100 \pm 5$ K/W. Assuming this value for R_{losses}, the h_{evap} for each experimental case can be determined.

Table 7.5: Calculations for Thermal Impedances of the Network

Thermal Resistance	**Description**	**Value**
R_{nat} [K/W]	Natural convection on PCB back	32
R_{sp} [K/W]	Spreading resistance in PCB	47.2
R_B [K/W]	Backside resistance	79.2
R_{ch} [K/W]	Natural convection at hot GaN device	4,806
R_{cc} [K/W]	Natural convection at cold sample	80
R_{cond} [K/W]	Condensation on sample	0.4
R_{rad} [K/W]	Radiation thermal resistance	1114

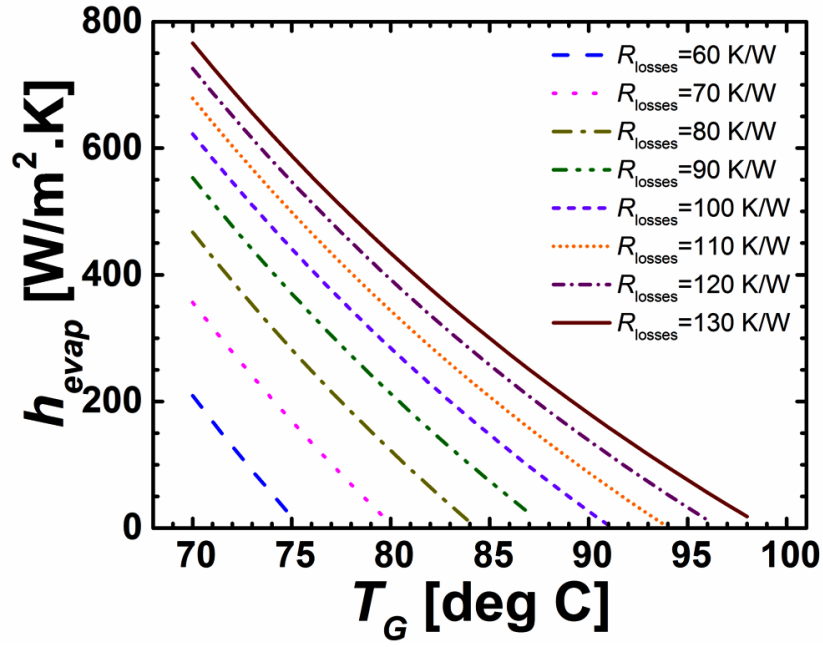

Figure 7.5: Evaporation HTC, h_{evap}, in terms of the GaN temperature for different values of R_{losses}.

7.7 Comparing Model and Experimental Results

The thermal resistance network of Fig. 7.1 was solved by inputting the relevant experimentally measured temperatures from Table 7.4 and solving for all of the relevant heat transfer pathways during circuit operation for the no-jumping, no-field jumping, and EFE jumping cases. This utilizes the previously calculated thermal impedance values from Table 7.5 and the estimation for R_{losses}. The bottom sections of Table 7.6 and Fig. 7.6 summarize the calculated results in each experimental case for the HTC of evaporation, h_{evap}, the temperature reduction due to thermal network on the front side of the PCB, q_f, and the heat flux due to the thermal network on the front side of the PCB, Ψ_f.

Although only modest GaN FET temperature decreases ($\approx$ 2 °C) were obtained by jumping-droplet cooling with EFE, the EFE condensation was shown to have significant impact on heat transfer. For these ambient experiments, EFE condensation enhanced the heat transfer from the hot spot by $\approx$ 200% compared to cooling without jumping and by $\approx$ 20% compared non-EFE jumping, respectively. The relatively low heat fluxes dissipated by this cooling approach were mainly due to the presence of NCGs in this ambient vapor environment. This 1 W/m^{2}K is comparable to heat flux achieved by very low flow rate air blowing across a well-designed heat sink for a GaN device.

As discussed in the seminal paper [98], even trace amounts of NCGs hinder heat transfer by creating a "blanket effect." These gases lower the partial pressure of the water vapor, which reduces the droplet condensation rate. The counterdiffusion of water vapor to the surface, coupled with the diffusion of NCGs away from the surface, significantly deteriorates the condensation heat transfer process, and hence decreases the effective surface-to-vapor temperature difference. This can account for a more than 99% reduction in heat transfer. Therefore, the removal of NCGs under a vacuum environment will facilitate higher heat transfer by promoting faster jumping-droplet condensation, which will accelerate the liquid to gas phase change-cooling process. Also, h_{cond} will increase to 100,000 W/m^{2}K in vacuum. Based on [76, 87, 98], the removal of NCGs alone should increase the number of jumping droplets reaching the GaN FET enough to improve the heat flux by two orders of magnitude to roughly 120 W/cm^2.

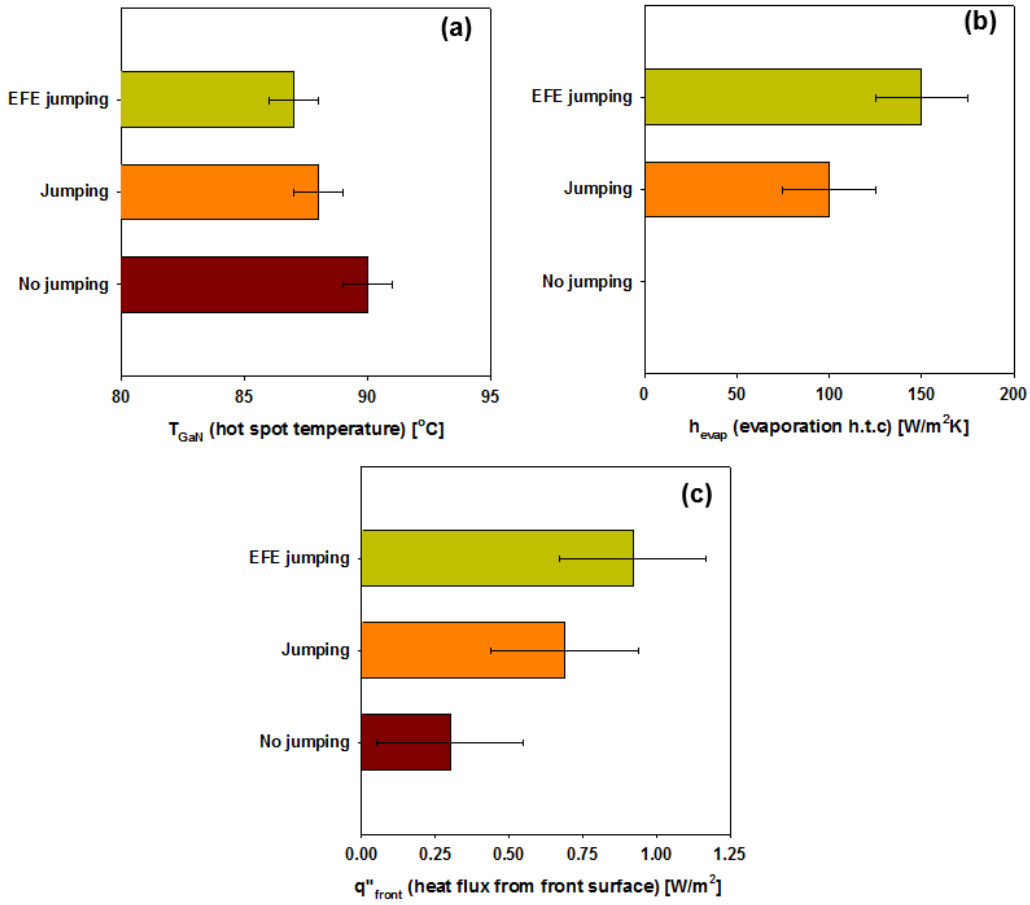

Figure 7.6: Examining how (a) hot spot temperature, (b) evaporation HTC, and (C) heat flux from front surface change based on experimental conditions.

7.8 Estimating Limits of EFE Jumping-Droplet Condensation Heat Transfer

To provide insight into the experimental results and to project the maximum potential of jumping-droplet cooling, we estimated the maximum possible thermal concentration of droplets that could reach a GaN FET using the image processing techniques coupled to previous condensation heat transfer measurements in pure vapor environments. Assuming that all of the departing droplets leave the superhydrophobic surface and reach the GaN device, the maximum jumping-droplet cooling heat flux is

$$\Psi = \Psi_c \frac{A_c}{A_g}, \tag{7.14}$$

where Ψ_c is the critical flooding heat flux for CuO superhydrophobic surfaces having conformal hydrophobic polymer coatings and A_c is the condenser area which is able to provide jumping droplets that move laterally from their jumping location to the GaN transistor. If L is the maximum horizontal distance that droplets can travel even with EFE, then this area can be found

Table 7.6: Quantitative Thermal Breakdown for the Key Single GaN Device Experiment and Analysis Parameters

Parameter [Units]	**No Jumping**	**Jumping**	**EFE Jumping**
Q_g [W]	1.6 ± 0.4	1.6 ± 0.4	1.6 ± 0.4
T_s [^{o}C]	5 ± 0.5	5 ± 0.5	5 ± 0.5
A_g [cm^2]	0.12 ± 0.01	0.12 ± 0.01	0.12 ± 0.01
h_{nat} [W/m^{2}K]	2 to 5	2 to 5	2 to 5
h_{cond} [W/m^{2}K]	100 to 1,000	100 to 1,000	100 to 1,000
h_{rad} [W/m^{2}K]	7.60	7.52	7.48
T_g [^{o}C]	90 ± 1	88 ± 1	87 ± 1
h_{evap} [W/m^{2}K]	≈ 0	100 ± 25	150 ± 25
q_f [W]	0.036 ± 0.03	0.082 ± 0.03	0.105 ± 0.03
Ψ_f [W/cm^2]	0.3 ± 0.25	0.69 ± 0.25	0.92 ± 0.25

from

$$A_c \approx 9A_g. \tag{7.15}$$

Assuming Ψ_c = 13 W/cm^2 based on this study, ΔT_g = 10 ^{o}C, and h_{evap} = 10,000 for conditions without NCGs, then Ψ_f = 120 W/cm^2 should be attainable in pure vapor environments for gap spacings of 3 mm for the GaN devices studied. This heat flux is comparable to the heat flux obtained from high flow rate air blowing across a well-designed heat sink for a GaN transistor.

CHAPTER 8

STEERABLE COOLING

To investigate the possibility of using jumping-droplet EFE condensation to achieve dynamic spatial-temporal control of cooling for mobile hot spots using the setup of Fig. 6.1, the experiments were repeated with the second revision of the PCB comprising two GaN devices spaced 3 mm apart in the horizontal direction and complete electrical isolation between the two transistors as described in in Section 6.2 and Appendix A. Two different methods were proposed for probing the capability of active, steerable cooling. Electric fields could be applied between the condensing surface and either an electrically floated circuit (directly to the transistor) or a guard ring (surrounding the transistor). The method of floating the source pins was found experimentally to be more effective than the external guard ring method in the ambient environment at attracting the droplets directly to the GaN devices.

Using the rear lighting scheme of Fig. 6.2a, long exposure images and videos of the jumping droplets were obtained for post-processing. Figure 8.1 reveals the impact of external electric fields on the trajectory of jumping droplets. If the electric field had not been present, then low exit trajectory droplets would not have followed the electric field lines leading to the GaN device as depicted in Fig. 8.1. The unique parabolic path in the right side of Fig. 8.1 also reveals how the droplets are accelerating toward the power devices due to the electric field. Accelerations between 3 and 6 m/s^2 for the droplets attracted by the electric fields were observed from measurements when a -100 V potential was applied across a 2.5 mm spacing between the cold plate and the GaN transistor. This corresponds to an electric field of -40 V/m pointing toward the GaN transistor. Thus, external electric fields will enhance the cooling capability by improving the rate and the number of droplets that reach the GaN FET by preventing droplet return due to gravitational forces as well as vapor flow entrainment back to the condensing surface.

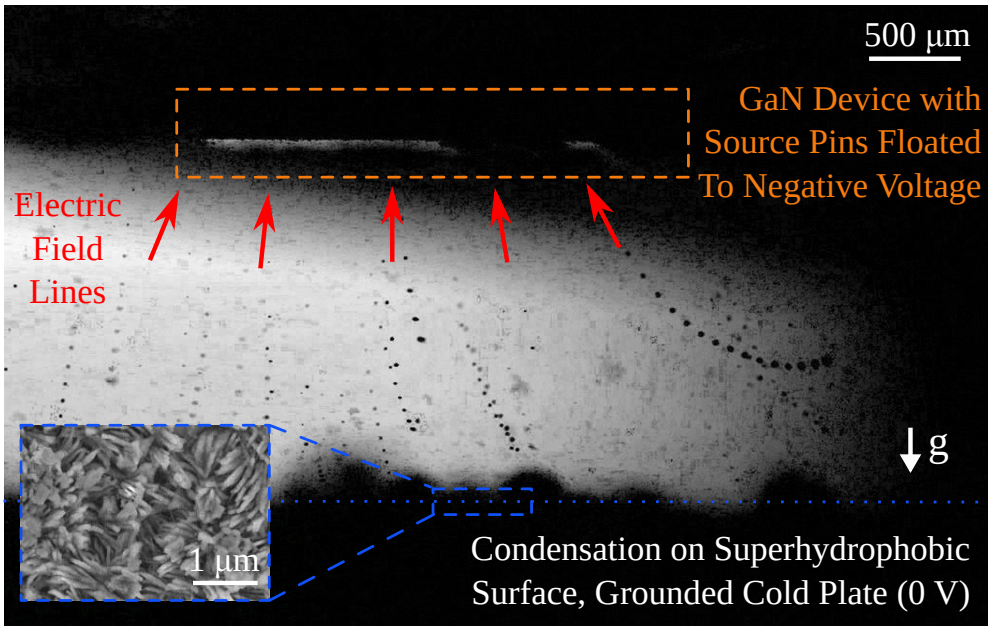

Figure 8.1: Composite image of several successive frames from a high speed video of electric-field-enhanced jumping-droplet condensation toward a GaN transistor with -100 V biased source pin with respect to the grounded superhydrophobic sample. The droplet trajectories clearly follow (are influenced by) the electric field lines, which are depicted by red arrows. Inset: top-view scanning electron micrograph of a C_4F_8 functionalized superhydrophobic CuO surface used in these experiments.

Electrically floating the source pin was found experimentally to direct the droplets closer to the GaN transistor than the external guard ring. Since the source pin approach involves electrically floating pins underneath approximately half of the total device surface as shown in Fig. 7.3b and Appendix A, the electric field lines attract all of the droplets directly toward the GaN FET. In contrast, some of the droplets attracted by the external guard ring would have to wick from the guard ring toward the package of the GaN device.

Building on these initial external electric field experiments, the two-transistor PCB was utilized to investigate the capacity of this technique for spatial and temporal steering of droplets toward specific GaN devices conducting current and generating hot spots on the PCB. By observing droplet trajectories through high speed imaging, the trajectories of droplets from the superhydrophobic surface to the GaN devices with no-field 8.2b, EFE condensation with the electric field biased towards only one GaN transistor (GaN #1) as

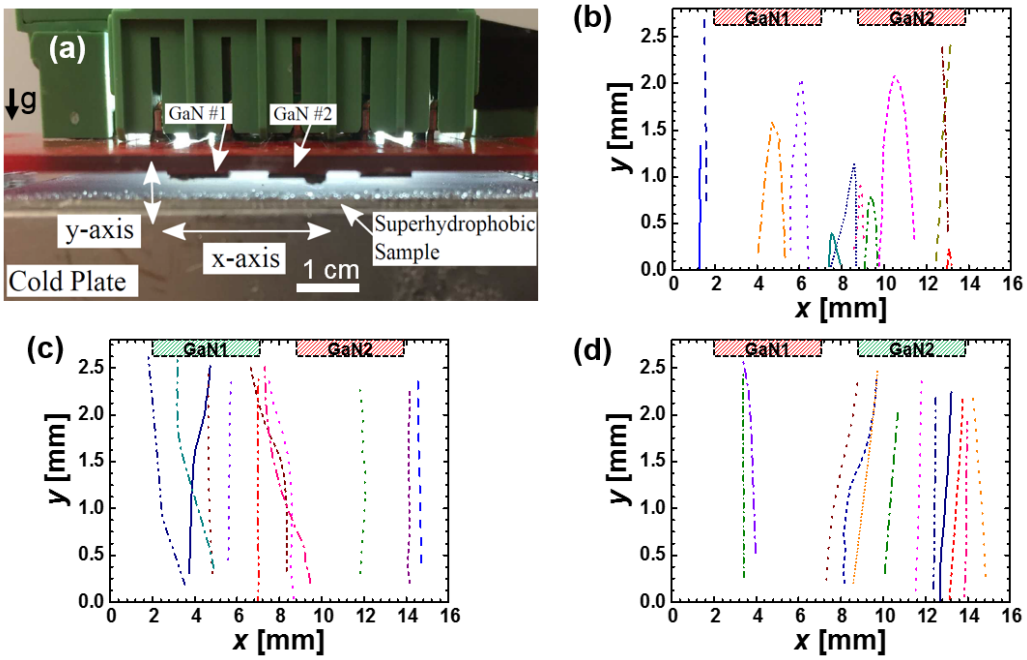

Figure 8.2: Demonstration of droplet steering for (a) experimental hardware (b) without electric field (shaded red), (c) electric field applied to the left GaN transistor (GaN #1, shaded green), and (d) electric field applied to the right GaN transistor (GaN #2, shaded green)

depicted in Fig. 8.2c or the electric field biased towards the other GaN FET (GaN #2) as in 8.2d were plotted. In contrast to Fig. 8.2b where no external electric fields are employed, Fig. 8.2c and 8.2d underscore how an external electric field dramatically increases the average number of droplet trajectories directed toward a specific GaN transistor. This is evidence of steerable cooling both spatially and temporally. The droplet trajectories in Fig. 8.2d, which appear to stop before reaching the GaN FET, are a good example of droplets leaving the plane of focus for the high resolution video camera. In this case, the droplets will reach the GaN device due to the external electric field.

The droplets' initial velocity, as measured from the videos, did not show a significant deviation from the inertial-capillary scaling, consistent with previous works on jumping droplets [79, 86, 87, 99, 100] that have deduced that the separation of charge on the superhydrophobic surface happens as a result of jumping, which leads to electrostatic interaction contributions only after the jump. The frequency of jumping was also not increased with the application of electric fields during the experiment. However, over the course of

long experiments, the reduced average droplet size on the surface will result in an increase in the number of droplets that are within the jumping range, causing an increased jumping frequency as an indirect effect of the applied field. Finally, Fig. 8.2 also demonstrates how EFE dramatically reduces the number of droplets that return to the cold plate immediately after jumping. In addition to the benefits of steerable cooling with EFE, this is another important feature of EFE jumping.

CHAPTER 9

CONCLUSION AND FUTURE WORK

This work outlines the first demonstration of the active cooling for electronic devices with EFE jumping-droplet condensation. For a worst-case scenario of a test environment with NCGs and droplets jumping against gravity, the jumping-droplet condensation was measured to have a significant impact on the cooling of conduction losses from a GaN transistor. Heat flux dissipations of 1 W/cm^2 in these ambient conditions were observed, which can be improved in the near-term to 120 W/cm^2 by removing the impact of NCGs using vacuum. As discussed in Chapter 5, this could be realized using a small, closed vacuum chamber that either acts as a heat spreader on top of the hot spot or encloses the hot spot. Yet, before one of these realizations of this advanced heat management system can be optimized, the theoretical limits of various design parameters should first be evaluated. Since a small, closed vacuum chamber would not allow for an examination of the jumping behavior inside based on different electrical and thermal conditions, the ambient experiments from this study should first be repeated inside of a large, vacuum compatible chamber with view ports for imaging and electrical feedthroughs for connections to the external power supplies. In this way, various performance as well as lifetime studies can be implemented with a simple method of obtaining quantitative measurements using the feedthroughs and view ports.

External electric fields were shown to be a mechanism to steer the jumping droplets toward specific hot spots for active cooling. This provides a framework for the development of active jumping-droplet-based vapor chambers and heat pipes capable of spatial and temporal thermal dissipation control. The utilization of droplet-jumping and active electric fields to locally cool mobile hot spots builds on state-of-the-art vapor chamber designs with several significant advantages as follows: (i) The electronics act directly as the evaporator and minimize thermal resistance as typically observed through the

utilization of thermal-interface-materials and channel walls. If integrated into a jumping-droplet vapor chamber geometry due to electrical isolation concerns, the mass flow rate of the liquid inside the jumping-droplet vapor chamber is dictated not by the height of the wick structure, but by the jumping frequency since the condenser liquid is returned through the vapor space. (ii) Spatial and temporal control of the jumping-droplet motion is possible with electric fields such that mobile hot spots can be sensed and cooled as needed. (iii) The low Bond number of the jumping droplets (Bo $\approx 10^{-3}$) allows operation independent of gravitational orientation. (iv) The out-of-plane jumping return is scalable and particularly suitable for planar systems, unlike conventional vapor chambers with capillary return along wicked walls, where longer liquid return paths are expected for devices of larger areas.

The EFE jumping-droplet cooling method demonstrated here is similar to, but fundamentally different from, prior jumping-droplet vapor chamber concepts in the literature. Spatial and temporal control of droplet motion is not possible in prior jumping-droplet vapor chamber concepts, whereas in the proposed device, active sensing of hot spots can be used as a feedback to locally direct droplets using electric fields. Furthermore, active application of electric fields may not be necessary, as the EFE concept developed here has future possibility of exploiting the inherent electric fields generated by the high voltage switching action (dv/dt) from power semiconductor devices to tailor the electric field to provide localized, directed cooling for the power devices. In addition to improved cooling, this effect may also realize a method to better equalize temperatures, a key design challenge for power sharing among parallel-connected devices. In the future, it would be interesting the investigate the performance of the device in pure vapor environments in vacuum due to: (i) the significant condensation thermal resistance added by NCGs, and (ii) the potential for droplet charge dissipation in the presence of NCGs. Furthermore, future studies should also investigate the durability of the superhydrophobic surfaces on internal sealed condenser devices, as any practical implementation will require a longevity of years if not decades.

EFE condensation was shown to enhance the heat transfer from the hot spot by $\approx 200\%$ compared to cooling without jumping and by $\approx 20\%$ compared to non-EFE jumping, respectively. Thus, these experimental observations complement additional theoretical results suggesting that an increase in the charge per droplet will have the most significant impact on further heat

flux enhancement since the effect of the electric field attrition force and area ratio can be increased ($A_c \approx L^2$). A secondary and more practical approach to increase the hot spot heat flux is to optimize the condenser-to-FET spacing or applied EFE voltage in order to attract more droplets. The experiments conducted here were limited to -100 V due to safety considerations; however, higher applied voltages are possible in closed systems. Additionally, the heat flux will improve for orientations where gravity helps the droplet trajectories.

All in all, this study demonstrated jumping-droplet hot spot cooling, whereby charged droplets jump between superhydrophobic copper oxide condensers and electrical circuits to cool local hot devices actively with evaporation. Through experiments and modeling, heat flux dissipations of 1 W/cm^2 were demonstrated, which can be improved in the near-term to 120 W/cm^2. The demonstrated spatial and temporal steering of droplets via external electric fields underscores the great promise of EFE jumping-droplet condensation as an active cooling scheme for mitigating hot spots in compact power electronics packages.

REFERENCES

[1] J. G. Kassakian and T. M. Jahns, "Evolving and emerging applications of power electronics in systems," *IEEE Journal of Emerging and Selected Topics in Power Electronics*, vol. 1, no. 2, pp. 47–58, June 2013. [Online]. Available: http://dx.doi.org/10.1109/JESTPE.2013.2271111

[2] B. Lequesne, "Automotive electrification the nonhybrid story," *IEEE Transactions on Transportation Electrification*, vol. 1, no. 1, pp. 40–53, June 2015. [Online]. Available: http://dx.doi.org/10.1109/TTE.2015.2426573

[3] X. E. Yu, Y. Xue, S. Sirouspour, and A. Emadi, "Microgrid and transportation electrification: A review," in *2012 IEEE Transportation Electrification Conference and Expo (ITEC)*, June 2012. [Online]. Available: http://dx.doi.org/10.1109/ITEC.2012.6243464 pp. 1–6.

[4] P. T. Krein, *Elements of Power Electronics*. Oxford University Press, 2015.

[5] R. J. Kaplar, J. C. Neely, D. L. Huber, and L. J. Rashkin, "Generation-after-next power electronics: Ultrawide-bandgap devices, high-temperature packaging, and magnetic nanocomposite materials," *IEEE Power Electronics Magazine*, vol. 4, no. 1, pp. 36–42, March 2017. [Online]. Available: http://dx.doi.org/10.1109/MPEL.2016.2643098

[6] J. Tsao, S. Chowdhury, M. Hollis, D. Jena, N. Johnson, K. Jones, R. Kaplar, S. Rajan, C. V. de Walle, E. Bellotti, C. Chua, R. Collazo, M. Coltrin, J. Cooper, K. Evans, S. Graham, T. Grotjohn, E. Heller, M. Higashiwaki, M. Islam, P. Juodawlkis, M. Khan, A. Koehlera, J. Leach, U. Mishra, R. Nemanich, R. Pilawa-Podgurski, J. Shealy, Z. Sitar, M. Tadjer, A.F.Witulski, M. Wraback, and J. Simmons, "Ultrawide-bandgap semiconductors: Research opportunities and challenges," *Advanced Electronic Materials*, 2017.

[7] J. W. Kolar, T. Friedli, F. Krismer, A. Looser, M. Schweizer, R. A. Friedemann, P. K. Steimer, and J. B. Bevirt, "Conceptualization and multiobjective optimization of the electric system of an airborne wind turbine," *IEEE Journal of Emerging and Selected Topics in Power Electronics*, vol. 1, no. 2, pp. 73–103, June 2013. [Online]. Available: https://doi.org/10.1109/JESTPE.2013.2269672

[8] S. Qin, A. J. Morrison, and R. C. N. Pilawa-Podgurski, "Enhancing micro-inverter energy capture with sub-module differential power processing," in *2014 IEEE Applied Power Electronics Conference and Exposition - APEC 2014*, March 2014. [Online]. Available: http://dx.doi.org/10.1109/APEC.2014.6803373 pp. 621–628.

[9] S. Qin and R. C. N. Pilawa-Podgurski, "Sub-module differential power processing for photovoltaic applications," in *2013 Twenty-Eighth Annual IEEE Applied Power Electronics Conference and Exposition (APEC)*, March 2013. [Online]. Available: http://dx.doi.org/10.1109/APEC.2013.6520193 pp. 101–108.

[10] T. Modeer, S. Norrga, and H. P. Nee, "Implementation and testing of high-power IGCT-based cascaded-converter cells," in *2014 IEEE Energy Conversion Congress and Exposition (ECCE)*, Sept 2014. [Online]. Available: https://doi.org/10.1109/ECCE.2014.6954135 pp. 5355–5359.

[11] T. Modeer, S. Norrga, and H. P. Nee, "Resonant test circuit for high-power cascaded converter submodules," in *2013 15th European Conference on Power Electronics and Applications (EPE)*, Sept 2013. [Online]. Available: https://doi.org/10.1109/EPE.2013.6631990 pp. 1–5.

[12] T. Modeer, S. Norrga, and H. P. Nee, "High-voltage tapped-inductor buck converter utilizing an autonomous high-side switch," *IEEE Transactions on Industrial Electronics*, vol. 62, no. 5, pp. 2868–2878, May 2015. [Online]. Available: https://doi.org/10.1109/TIE.2014.2365157

[13] E. Candan, D. Heeger, P. S. Shenoy, and R. C. N. Pilawa-Podgurski, "A series-stacked power delivery architecture with hot-swapping for high-efficiency data centers," in *2015 IEEE Energy Conversion Congress and Exposition (ECCE)*, Sept 2015. [Online]. Available: http://dx.doi.org/10.1109/ECCE.2015.7309740 pp. 571–578.

[14] P. S. Shenoy, K. A. Kim, B. B. Johnson, and P. T. Krein, "Differential power processing for increased energy production and reliability of photovoltaic systems," *IEEE Transactions on Power Electronics*, vol. 28, no. 6, pp. 2968–2979, June 2013. [Online]. Available: http://dx.doi.org/10.1109/TPEL.2012.2211082

[15] E. Candan, D. Heeger, P. Shenoy, and R. Pilawa-Podgurski, "Hot-swapping analysis and implementation of series-stacked server power delivery architectures," *IEEE Transactions on Power Electronics*, 2016. [Online]. Available: http://dx.doi.org/10.1109/TPEL.2016.2639519

[16] E. Candan, D. Heeger, P. Shenoy, and R. Pilawa-Podgurski, "A series-stacked power delivery architecture with isolated differential power conversion for data centers," *IEEE Transactions on Power Electronics*, vol. 31, no. 5, pp. 3690–3703, May 2016. [Online]. Available: http://dx.doi.org/10.1109/TPEL.2015.2464805

[17] E. Candan, A. Stillwell, and R. C. N. Pilawa-Podgurski, "A reliability assessment of series-stacked servers with server-to-bus differential power processing," in *2016 IEEE International Telecommunications Energy Conference (INTELEC)*, Oct 2016. [Online]. Available: http://dx.doi.org/10.1109/INTLEC.2016.7749094 pp. 1–7.

[18] A. Shehabi, S. Smith, D. Sartor, R. Brown, M. Herrlin, J. Koomey, E. Masanet, N. Horner, I. Azevedo, and W. Lintner, "United States data center energy usage report from Lawrence Berkeley National Laboratory," 2016.

[19] M. O'Keefe and K. Bennion, "A comparison of hybrid electric vehicle power electronics cooling options," in *2007 IEEE Vehicle Power and Propulsion Conference*, Sept 2007. [Online]. Available: http://dx.doi.org/10.1109/VPPC.2007.4544110 pp. 116–123.

[20] B. Whitaker, A. Barkley, Z. Cole, B. Passmore, D. Martin, T. R. McNutt, A. B. Lostetter, J. S. Lee, and K. Shiozaki, "A high-density, high-efficiency, isolated on-board vehicle battery charger utilizing silicon carbide power devices," *IEEE Transactions on Power Electronics*, vol. 29, no. 5, pp. 2606–2617, May 2014. [Online]. Available: http://dx.doi.org/10.1109/TPEL.2013.2279950

[21] U. Anwar, H. Kim, H. Chen, R. Erickson, D. Maksimovic, and K. K. Afridi, "A high power density drivetrain-integrated electric vehicle charger," in *2016 IEEE Energy Conversion Congress and Exposition (ECCE)*, Sept 2016. [Online]. Available: http://dx.doi.org/10.1109/ECCE.2016.7854694 pp. 1–8.

[22] D. Selvey, "Overview of the unique requirements and challenges for power electronics in mining equipment," Caterpillar Inc., Tech. Rep., 2016. [Online]. Available: http://www.psma.com/tech-forums-transportation-power-electronics/presentations/4217

[23] B. Busco, P. Marino, M. Porzio, R. Schiavo, and F. Vasca, "Digital control and simulation for power electronic apparatus in dual voltage railway locomotive," *IEEE Transactions on Power Electronics*, vol. 18, no. 5, pp. 1146–1157, Sept 2003. [Online]. Available: http://dx.doi.org/10.1109/TPEL.2003.816198

[24] C. R. Akli, X. Roboam, B. Sareni, and A. Jeunesse, "Energy management and sizing of a hybrid locomotive," in *2007 European Conference on Power Electronics and Applications*, Sept 2007. [Online]. Available: http://dx.doi.org/10.1109/EPE.2007.4417333 pp. 1–10.

[25] P. H. Desai and G. Wiegner, "Evaluation of freon modules for power electronics designed for a locomotive traction drive," *IEEE Transactions on Industry Applications*, vol. 26, no. 3, pp. 394–400, May 1990. [Online]. Available: http://dx.doi.org/10.1109/10.1109/28.55968

[26] M. M. Bakran and H. G. Eckel, "Power electronics technologies for locomotives," in *2007 Power Conversion Conference - Nagoya*, April 2007. [Online]. Available: http://dx.doi.org/10.1039/10.1109/PCCON.2007.373142 pp. 1362–1368.

[27] T. Ericsen, "The ship power electronic revolution issues and answers," in *2008 55th IEEE Petroleum and Chemical Industry Technical Conference*, Sept 2008. [Online]. Available: http://dx.doi.org/10.1109/PCICON.2008.4663984 pp. 1–11.

[28] G. Sulligoi, A. Vicenzutti, and R. Menis, "All-electric ship design from electrical propulsion to integrated electrical and electronic power systems," *IEEE Transactions on Transportation Electrification*, vol. 2, no. 4, pp. 507–521, Dec 2016. [Online]. Available: http://dx.doi.org/10.1109/TTE.2016.2598078

[29] J. E. Huber and J. W. Kolar, "Optimum number of cascaded cells for high-power medium-voltage acdc converters," *IEEE Journal of Emerging and Selected Topics in Power Electronics*, vol. 5, no. 11, pp. 213–232, March 2017. [Online]. Available: http://dx.doi.org/10.1109/JESTPE.2016.2605702

[30] T. J. McCoy and J. V. Amy, "The state-of-the-art of integrated electric power and propulsion systems and technologies on ships," in *2009 IEEE Electric Ship Technologies Symposium*, April 2009. [Online]. Available: http://dx.doi.org/10.1109/ESTS.2009.4906534 pp. 340–344.

[31] S. D. Sudhoff, S. D. Pekarek, R. R. Swanson, V. S. Duppalli, D. C. Horvath, A. E. Kasha, R. Lin, B. D. Marquet, P. R. O'Regan, H. Suryanarayana, and Y. Yan, "A reduced scale naval dc microgrid to support electric ship research and development," in *2015 IEEE Electric Ship Technologies Symposium (ESTS)*, June 2015. [Online]. Available: http://dx.doi.org/10.1109/ESTS.2015.7157911 pp. 464–471.

[32] N. H. Doerry and D. H. Clayton, "Shipboard electrical power quality of service," in *IEEE Electric Ship Technologies Symposium, 2005.*, July 2005. [Online]. Available: http://dx.doi.org/10.1109/ESTS.2005.1524688 pp. 274–279.

[33] N. Madavan, C. Bowman, P. Kascak, A. Jankovsky, and R. Jansen, "A NASA perspective on electric propulsion technologies for commercial aviation," *Workshop on Technology Roadmap for Large Electric MachinesUniversity of Illinois Urbana-Champaign*, 2016. [Online]. Available: https://machineroadmap.ece.illinois.edu/files/2016/04/Madavan.pdf

[34] G. V. Brown, "Weights and efficiencies of electric components of a turboelectric aircraft propulsion system," *49th AIAA Aerospace Sciences Meeting including the New Horizons Forum and Aerospace Exposition*, January 2011. [Online]. Available: http://dx.doi.org/10.2514/6.2011-225

[35] R. Jansen, G. V. Brown, J. L. Felder, and K. P. Duffy, "Weights and efficiencies of electric components of a turboelectric aircraft propulsion system," *51st AIAA/SAE/ASEE Joint Propulsion Conference, Propulsion and Energy Forum*, 2015. [Online]. Available: http://dx.doi.org/10.2514/6.2015-3890

[36] R. Jansen, C. Bowman, and A. Jankovsky, "Sizing power components of an electrically driven tail cone thruster and a range extender," *16th AIAA Aviation Technology, Integration, and Operations Conference in Washington D.C.*, 2016. [Online]. Available: http://dx.doi.org/10.2514/6.2016-3766

[37] M. Hathaway, R. D. Rosario, and N. Madavan, "NASA fixed wing project propulsion research and technology development activities to reducethrust specific energy consumption," *49th Joint Propulsion Conference and Exhibitcosponsored by AIAA, ASME, SAE, and ASEE*, July 14-17 2013. [Online]. Available: https://ntrs.nasa.gov/search.jsp?R=20140008324

[38] J. W. Kolar, U. Drofenik, J. Biela, M. L. Heldwein, H. Ertl, T. Friedli, and S. D. Round, "Pwm converter power density barriers," in *2007 Power Conversion Conference - Nagoya*, April 2007. [Online]. Available: http://dx.doi.org/10.1109/PCCON.2007.372914 pp. P–9–P–29.

[39] J. W. Kolar, J. Biela, S. Waffler, T. Friedli, and U. Badstuebner, "Performance trends and limitations of power electronic systems," in *2010 6th International Conference on Integrated Power Electronics Systems*, March 2010, pp. 1–20.

[40] Y. Lei, C. Barth, S. Qin, W.-C. Liu, I. Moon, A. Stillwell, D. Chou, T. Foulkes, Z. Ye, Z. Liao, and R. Pilawa-Podgurski, "A 2 kW, single-phase, 7-level, GaN inverter with an active energy buffer achieving 216 W/in^3 power density and 97.6% peak efficiency," in *Applied Power Electronics Conference and Exposition (APEC), 2016 IEEE*, 2016. [Online]. Available: http://dx.doi.org/10.1109/APEC.2016.7468068 pp. 1512–1519.

[41] Y. Lei, C. Barth, S. Qin, W. C. Liu, I. Moon, A. Stillwell, D. Chou, T. Foulkes, Z. Ye, Z. Liao, and R. Pilawa-Podgurski, "A 2 kw, single-phase, 7-level flying capacitor multilevel inverter with an active energy buffer," *IEEE Transactions on Power Electronics*, 2017. [Online]. Available: http://dx.doi.org/10.1109/TPEL.2017.2650140

[42] S. Qin, Y. Lei, C. Barth, W. C. Liu, and R. C. N. Pilawa-Podgurski, "A high power density series-stacked energy buffer for power pulsation decoupling in single-phase converters," *IEEE Transactions on Power Electronics*, vol. 32, no. 6, pp. 4905–4924, June 2017. [Online]. Available: http://dx.doi.org/10.1109/TPEL.2016.2601309

[43] T. Modeer, C. Barth, N. Pallo., W. Chung, T. Foulkes, and R. Pilawa-Podgurski, "Design of a GaN-based, 9-level flying capacitor multilevel inverter with low inductance layout," in *IEEE Applied Power Electronics Conference and Exposition (APEC)*, March 2017.

[44] T. Modeer, C. Barth, Y. Lei, and R. Pilawa-Podgurski, "An analytical method for evaluating the power density of multilevel converters," in *2016 IEEE 17th Workshop on Control and Modeling for Power Electronics (COMPEL)*, June 2016. [Online]. Available: http://dx.doi.org/10.1109/COMPEL.2016.7556759 pp. 1–5.

[45] J. Colmenares, T. Foulkes, C. Barth, T. Modeer, and R. C. N. Pilawa-Podgurski, "Experimental characterization of enhancement mode gallium-nitride power field-effect transistors at cryogenic temperatures," in *2016 IEEE 4th Workshop on Wide Bandgap Power Devices and Applications (WiPDA)*, Nov 2016. [Online]. Available: http://dx.doi.org/10.1109/WiPDA.2016.7799923 pp. 129–134.

[46] C. Barth, J. Colmenares, T. Foulkes, K. Coulson, J. Sotelo, T. Modeer, N. Miljkovic, , and R. Pilawa-Podgurski, "Experimental evaluation of a 1 kw, single-phase, 3-level gallium-nitride inverter in extreme cold environmnet," in *IEEE Applied Power Electronics Conference and Exposition (APEC)*, March 2017.

[47] M. Kasper, D. Bortis, G. Deboy, and J. Kolar, "Design of a highly efficient and very compact isolated acdc telecom power supply module based on the multi-cell isop converter approach," *IEEE Transactions on Power Electronics*, 2017. [Online]. Available: http://dx.doi.org/10.1109/TPEL.2016.2633334

[48] C. B. Barth, T. Foulkes, W. H. Chung, T. Modeer, P. Assem, Y. Lei, and R. C. N. Pilawa-Podgurski, "Design and control of a GaN-based, 13-level, flying capacitor multilevel inverter," in *2016 IEEE 17th Workshop on Control and Modeling for Power Electronics (COMPEL)*, June 2016. [Online]. Available: http://dx.doi.org/10.1109/COMPEL.2016.7556770 pp. 1–6.

[49] Z. Liao, Y. Lei, and R. C. N. Pilawa-Podgurski, "A GaN-based flying-capacitor multilevel boost converter for high step-up conversion," in *2016 IEEE Energy Conversion Congress and Exposition (ECCE)*, Sept 2016. [Online]. Available: http://dx.doi.org/10.1109/ECCE.2016.7854684 pp. 1–7.

[50] J. Colmenares, D. Peftitsis, J. Rabkowski, D. P. Sadik, G. Tolstoy, and H. P. Nee, "High-efficiency 312-kVA three-phase inverter using parallel connection of silicon carbide MOSFET power modules," *IEEE Transactions on Industry Applications*, vol. 51, no. 6, pp. 4664–4676, Nov 2015. [Online]. Available: http://dx.doi.org/10.1109/TIA.2015.2456422

[51] A. Stillwell, D. Heeger, C. Meyer, S. Bedair, and R. C. N. Pilawa-Podgurski, "An interleaved 1-to-6 step-up resonant switched-capacitor converter utilizing split-phase control," in *2016 IEEE Energy Conversion Congress and Exposition (ECCE)*, Sept 2016. [Online]. Available: http://dx.doi.org/10.1109/ECCE.2016.7854854 pp. 1–8.

[52] J. W. Kolar, D. Bortis, and D. Neumayr, "The ideal switch is not enough," in *2016 28th International Symposium on Power Semiconductor Devices and ICs (ISPSD)*, June 2016. [Online]. Available: http://dx.doi.org/10.1109/ISPSD.2016.7520767 pp. 15–22.

[53] M. Hartmann, S. D. Round, H. Ertl, and J. W. Kolar, "Digital current controller for a 1 mhz, 10 kW Three-Phase vienna rectifier," *IEEE Transactions on Power Electronics*, vol. 24, no. 11, pp. 2496–2508, Nov 2009. [Online]. Available: http://dx.doi.org/10.1109/TPEL.2009.2031437

[54] B. B. Macy, Y. Lei, and R. C. N. Pilawa-Podgurski, "A 1.2 mhz, 25 v to 100 v gan-based resonant dickson switched-capacitor converter with 1011 w/in3 (61.7 kw/l) power density," in *IEEE Applied Power Electronics Conference and Exposition (APEC)*, March 2015. [Online]. Available: http://dx.doi.org/10.1109/APEC.2015.7104542 pp. 1472–1478.

[55] M. Schweizer, T. Friedli, and J. W. Kolar, "Comparative evaluation of advanced three-phase three-level inverter/converter topologies against two-level systems," *IEEE Transactions on Industrial Electronics*, vol. 60, no. 12, pp. 5515–5527, Dec 2013. [Online]. Available: http://dx.doi.org/10.1109/TIE.2012.2233698

[56] J. Colmenares, S. Kargarrazi, H. Elahipanah, H. P. Nee, and C. M. Zetterling, "High-temperature passive components for extreme environments," in *2016 IEEE 4th Workshop on Wide Bandgap Power Devices and Applications (WiPDA)*, Nov 2016. [Online]. Available: http://dx.doi.org/10.1109/WiPDA.2016.7799951 pp. 271–274.

[57] D. P. Sadik, K. Kostov, J. Colmenares, F. Giezendanner, P. Ranstad, and H. P. Nee, "Analysis of parasitic elements of sic power modules with special emphasis on reliability issues," *IEEE Journal of Emerging and Selected Topics in Power Electronics*, vol. 4, no. 3, pp. 988–995, Sept 2016. [Online]. Available: http://dx.doi.org/10.1109/JESTPE.2016.2585666

[58] D. P. Sadik, H. P. Nee, F. Giezendanner, and P. Ranstad, "Humidity testing of sic power mosfets," in *2016 IEEE 8th International Power Electronics and Motion Control Conference (IPEMC-ECCE Asia)*, May 2016. [Online]. Available: http://dx.doi.org/10.1109/IPEMC.2016.7512796 pp. 3131–3136.

[59] U. Drofenik and J. W. Kolar, "Thermal power density barriers of converter systems," in *5th International Conference on Integrated Power Electronics Systems*, March 2008, pp. 1–5.

[60] P. Tannous, S. Peddada, J. Allison, T. Foulkes, R. C. N. Pilawa-Podgurski, and A. Alleyne, "Dynamic temperature estimation of power electronics systems," *2017 IEEE American Control Conference*, 2017.

[61] Y. Lei, Z. Ye, and R. C. N. Pilawa-Podgurski, "A GaN-based 97% efficient hybrid switched-capacitor converter with lossless regulation capability," in *2015 IEEE Energy Conversion Congress and Exposition (ECCE)*, Sept 2015. [Online]. Available: http://dx.doi.org/10.1109/ECCE.2015.7310262 pp. 4264–4270.

[62] A. Stillwell, Y. Lei, and R. C. N. Pilawa-Podgurski, "A method to extract low-voltage auxiliary power from a flying capacitor multi-level converter," in *2016 IEEE 17th Workshop on Control and Modeling for Power Electronics (COMPEL)*, June 2016. [Online]. Available: http://dx.doi.org/10.1109/COMPEL.2016.7556747 pp. 1–8.

[63] T. Foulkes, J. Oh, P. Birbarah, J. Neely, N. Miljkovic, and R. Pilawa-Podgurski, "Active hot spot cooling of GaN transistors with electric field enhanced jumping droplet condensation," *IEEE Applied Power Electronics Conference and Exposition (APEC)*, March 2017.

[64] J. Oh, P. Birbarah, T. Foulkes, S. Yin, M. Rentauskas, J. Neely, R. Pilawa-Podgurski, and N. Miljkovic, "Jumping-droplet electronics hot-spot cooling," *Applied Physics Letters*, vol. 110, March 2017. [Online]. Available: doi: http://dx.doi.org/10.1063/1.4979034

[65] N. Miljkovic, D. Preston, R. Enright, and E. Wang, "Electrostatic charging of jumping droplets," *Nature Communications*, vol. 4, pp. 1–9, September 2013. [Online]. Available: http://dx.doi.org/10.1038/ncomms3517

[66] D. Quere, "Wetting and roughness," *Annual Review of Materials Research*, vol. 38, pp. 71–99, April 2008. [Online]. Available: http://dx.doi.org/10.1146/annurev.matsci.38.060407.132434

[67] K. Liu and L. Jiang, "Bio-inspired self-cleaning surfaces," *Annual Review of Materials Research*, vol. 42, pp. 231–263, May 2012. [Online]. Available: http://dx.doi.org/10.1146/annurev-matsci-070511-155046

[68] S. Chavan, J. Carpenter, M. Nallapaneni, J. Y. Chen, and N. Miljkovic, "Bulk water freezing dynamics on superhydrophobic surfaces," *Applied Physics Letters*, vol. 110, no. 4, January 2017. [Online]. Available: doi: http://dx.doi.org/10.1063/1.4974296

[69] L. Mishchenko, B. Hatton, V. Bahadur, J. Taylor, T. Krupenkin, and J. Aizenberg, "Design of ice-free nanostructured surfaces based on repulsion of impacting water droplets," *ACS Nano*, vol. 4, no. 12, pp. 7699–7707, December 2010. [Online]. Available: http://dx.doi.org/10.1021/nn102557p

[70] L. Cao, A. Jones, V. Sikka, J. Wu, and D. Gao, "Anti-icing superhydrophobic coatings," *Langmuir*, vol. 25, no. 21, p. 1244412448, October 2009. [Online]. Available: http://dx.doi.org/10.1021/la902882b

[71] H. Cha, C. Xu, J. Sotelo, J. Chun, Y. Yokoyama, R. Enright, and N. Miljkovic, "Coalescence-induced nanodroplet jumping," *Physical Review Fluids*, vol. 1, no. 6, October 2016. [Online]. Available: DOI:https://doi.org/10.1103/PhysRevFluids.1.064102

[72] N. Miljkovic, R. Enright, and E. N. Wang, "Liquid freezing dynamics on hydrophobic and superhydrophobic surfaces," *J. Heat Transfer*, vol. 134, no. 8, June 27 2012. [Online]. Available: http://dx.doi.org/10.1115/1.4006675

[73] R. Andre, F. Natalio, M. Tahir, R. Berger, and W. Tremel, "Self-cleaning antimicrobial surfaces by bio-enabled growth of SnO2 coatings on glass," *Nanoscale*, vol. 5, pp. 3447–3456, February 2013. [Online]. Available: http://dx.doi.org/10.1039/C3NR00007A

[74] N. Miljkovic, D. Preston, R. Enright, and E. Wang, "Jumping-droplet electrostatic energy harvesting," *Applied Physics Letters*, vol. 105, pp. 013 111–013 115, 2014. [Online]. Available: http://dx.doi.org/10.1063/1.4886798

[75] N. Miljkovic, R. Enright, and E. Wang, "Modeling and optimization of superhydrophic condensation," *Journal of Heat Transfer*, vol. 135, pp. 1 110 041–1 100 414, 2013. [Online]. Available: http://dx.doi.org/10.1115/1.4024597

[76] R. Enright, N. Miljkovic, J. Sprittles, K. Nolan, R. Mitchell, and E. Wang, "How coalescing droplets jump," *ACS Nano*, vol. 8, no. 10, pp. 10 352–10 362, 2014. [Online]. Available: http://dx.doi.org/10.1021/nn503643m

[77] J. B. Boreyko and C.-H. Chen, "Vapor chambers with jumping-drop liquid return from superhydrophobic condensers," *International Journal of Heat and Mass Transfer*, vol. 61, p. 409418, June 2013. [Online]. Available: http://dx.doi.org/10.1016/j.ijheatmasstransfer.2013.01.077

[78] J. B. Boreyko, Y. Zhao, and C.-H. Chen, "Planar jumping-drop thermal diodes," *Appl. Phys. Lett*, vol. 99, no. 23, November 2011. [Online]. Available: doi: http://dx.doi.org/10.1063/1.3666818

[79] N. Miljkovic and E. Wang, "Condensation heat transfer on superhydrophobic surfaces," *MRS Bulletin*, vol. 38, no. 5 (Interfacial Materials with Special Wettability), pp. 397–406, May 2013. [Online]. Available: https://doi.org/10.1557/mrs.2013.103

[80] S. Chavan, H. Cha, D. Orejon, K. Nawaz, N. Singla, Y. Yeung, D. Park, D. Kang, Y. . Chang, Y. Takata, and N. Miljkovic, "Heat transfer through a condensate droplet on hydrophobic and nanostructured superhydrophobic surfaces." *Langmuir*, vol. 32, no. 31, pp. 7774–7787, July 2016. [Online]. Available: https://doi.org/10.1021/acs.langmuir.6b01903

[81] Pliny the Elder, *Natural History: A Selection*, transl. ed. JF. Healey, Ed. Penguin, 2004.

[82] J. Bush, D. Hu, and M. Prakash, "The integument of water-walking arthropods: Form and function," *Advances in Insect Physiology*, vol. 34, pp. 117–192, 2007. [Online]. Available: http://doi.org/10.1016/S0065-2806(07)34003-4

[83] N. Miljkovic, R. Enright, Y. Nam, K. Lopex, N. Dou, J. Sack, and E. Wang, "Jumping droplet-enhanced condensation on scalable superhydrophic nanostructured surfaces," *Nano Letters*, vol. 13, pp. 179–187, 2012. [Online]. Available: http://dx.doi.org/10.1021/nl303835d

[84] R. Enright, N. Miljkovic, J. Alvarado, K. Kim, and J. Rose, "Dropwise condensation on micro and nanostructured surfaces," *Nanoscale and Microscale Thermophysical Engineering*, vol. 18, pp. 223–250, 2014. [Online]. Available: http://dx.doi.org/10.1080/15567265.2013.862889

[85] N. Miljkovic, R. Enright, and E. Wang, "Effect of droplet morphology on growth dynamics and heat transfer during condensation on superhydrophobic nanostructured surfaces," *ACS Nano*, vol. 6, no. 2, pp. 1776–1785, 2012. [Online]. Available: http://dx.doi.org/10.1021/nn205052a

[86] J. Boreyko and C. Chen, "Self-propelled dropwise condensate on superhydrophobic surfaces," *Phys. Rev. Lett.*, vol. 103, October 2009. [Online]. Available: https://doi.org/10.1103/PhysRevLett.103.184501

[87] P. Birbarah, Z. Li, A. Pauls, and N. Miljkovic, "A comprehensive modeling of electric-field-enhanced jumping-droplet condensation on superhydrophic surfaces," *Langmuir*, vol. 31, pp. 7885–7896, 2015. [Online]. Available: http://dx.doi.org/10.1021/acs.langmuir.5b01762

[88] J. Strydom, D. Reusch, S. Colino, and A. Nakata, "Using enhancement mode GaN-on-silicon power FETs," *EPC Application Note AN003*, 2014.

[89] E. P. C. Corporation, "EPC2034 - Enhancement mode power transistor (eGaN FET datasheet)," 2016.

[90] A. Stupar, U. Drofenik, and J. W. Kolar, "Optimization of phase change material heat sinks for low duty cycle high peak load power supplies," *IEEE Transactions on Components, Packaging, Manufacturing Technology*, vol. 2, no. 1, pp. 102–115, Jan 2012. [Online]. Available: http://dx.doi.org/10.1109/TCAPT.2004.825758

[91] S. Krishnan and S. V. Garimella, "Analysis of a phase change energy storage system for pulsed power dissipation," *IEEE Transactions on Components and Packaging Technologies*, vol. 27, no. 1, pp. 191–199, March 2004. [Online]. Available: http://dx.doi.org/10.1109/TCAPT.2004.825758

[92] S. Krishnan, S. V. Garimella, and S. S. Kang, "A novel hybrid heat sink using phase change materials for transient thermal management of electronics," *IEEE Transactions on Components and Packaging Technologies*, vol. 28, no. 2, pp. 281–289, June 2005. [Online]. Available: http://dx.doi.org/10.1109/TCAPT.2005.848534

[93] E. Pennewitz, M. Schilling, T. Kruspe, S. Jung, and A. Ruehs, "Active cooling of downhole instrumentation for drilling in deep geothermal reservoirs," in *Instrumentation and Measurement Technology Conference (I2MTC), 2012 IEEE International*, May 2012. [Online]. Available: http://dx.doi.org/10.1109/I2MTC.2012.6229454 pp. 600–603.

[94] A. Sinha and Y. Joshi, "Downhole electronics cooling using a thermoelectric device and heat exchanger arrangement," *J. Electron. Packaging*, vol. 133, no. 4, 2011. [Online]. Available: http://dx.doi.org/10.1115/1.4005290

[95] T. Wijekoon, L. Empringham, P. W. Wheeler, J. C. Clare, C. Whitley, and G. Towers, "Aircraft electrical landing gear actuation using dual-output power converter with mutual power circuit components," in *Applied Power Electronics Conference and Exposition, 2009. APEC 2009. Twenty-Fourth Annual IEEE*, Feb 2009. [Online]. Available: http://dx.doi.org/10.1109/APEC.2009.4802826 pp. 1263–1268.

[96] N. Miljkovic, D. Preston, R. Enright, S. Adera, Y. Nam, and E. Wang, "Jumping droplet dynamics on scalable nanostructured superhydrophobic surfaces," *Journal of Heat Transfer*, vol. 135, p. 1, August 2013. [Online]. Available: http://dx.doi.org/10.1115/1.4024189

[97] Y. Nam and Y. S. Ju, "A comparative study of the morphology and wetting characteristics of micro/nanostructured cu surfaces for phase change heat transfer applications," *Journal of Adhesion Science and Technology*, vol. 27, no. 20, pp. 2163–2176, 2012. [Online]. Available: http://dx.doi.org/10.1080/01694243.2012.697783

[98] E. Sparrow and S. Lin, "Condensation heat transfer in the presence of a noncondensable gas," *ASME. J. Heat Transfer*, vol. 86, pp. 430–436, 1964. [Online]. Available: http://dx.doi.org/10.1115/1.3688714

[99] N. Miljkovic, D. Preston, R. Enright, and E. Wang, "Electric-field-enhanced condensation on superhydrophic nanostructured surfaces," *ACS Nano*, vol. 7, no. 12, pp. 11 043–11 054, 2013. [Online]. Available: http://dx.doi.org/10.1021/nn404707j

[100] A. Shahriari, P. Birbarah, J. Oh, N. Miljkovic, and V. Bahadur, "Electric field based control and enhancement of boiling and condensation," *Nanoscale and Microscale Thermophysical Engineering*, pp. 1–20, October 27 2016. [Online]. Available: http://dx.doi.org/10.1080/15567265.2016.1253630

APPENDIX A

HARDWARE SCHEMATICS

The following figures provide the schematics and PCB artwork for revision A and revision B of this project. For revision A, three GaN devices share a common source pin connection, but have separate guard rings. In contrast, revision B reduced the number of active devices to two GaN transistors and separated their source connections. The guard rings were also included in revision B. Gerber files generated by KiCad EDA, an open source circuit layout tool, can be viewed using the free software, Gerbv (Gerber Viwer Version 2.6.1).

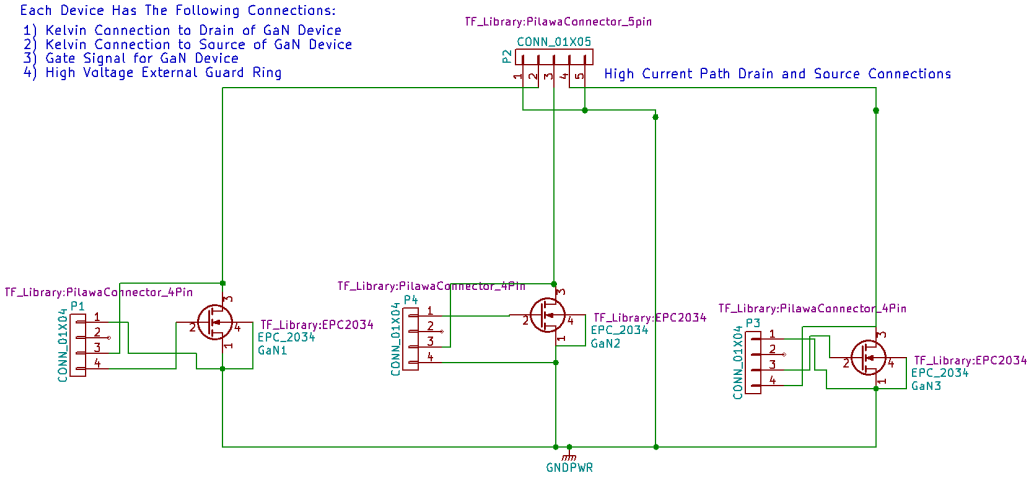

Figure A.1: KiCad schematic for revision A.

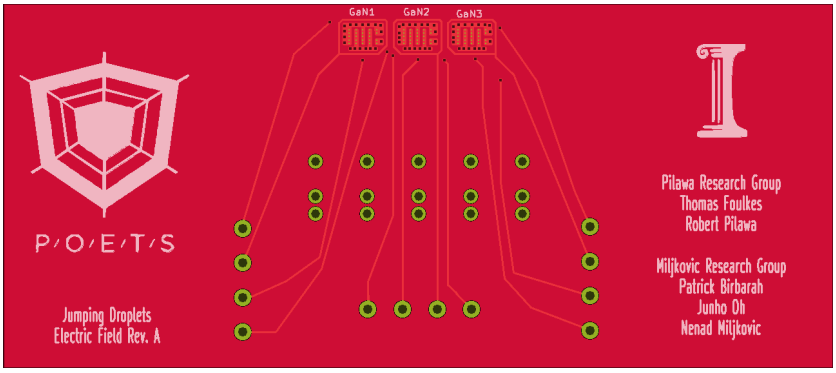

Figure A.2: PCB artwork for drill locations and for the front copper, front mask, and front silk layers of revision A.

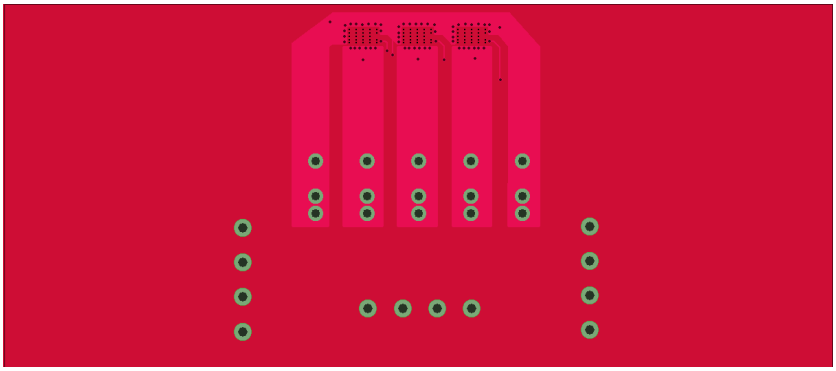

Figure A.3: PCB artwork for drill locations and for the back copper, back mask, and back silk layers of revision A.

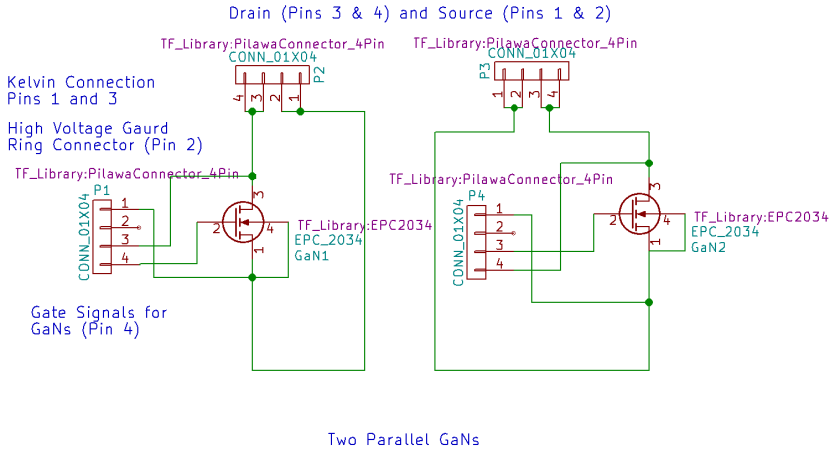

Figure A.4: KiCad schematic for revision B.

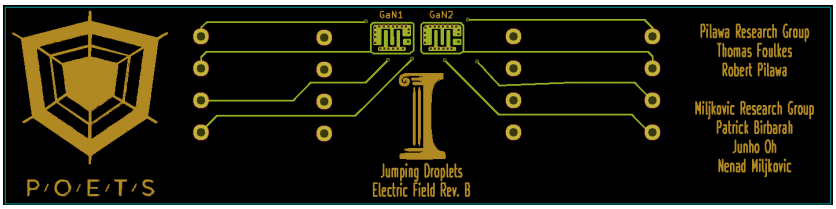

Figure A.5: PCB artwork for drill locations and for the front copper, front mask, and front silk layers of revision B.

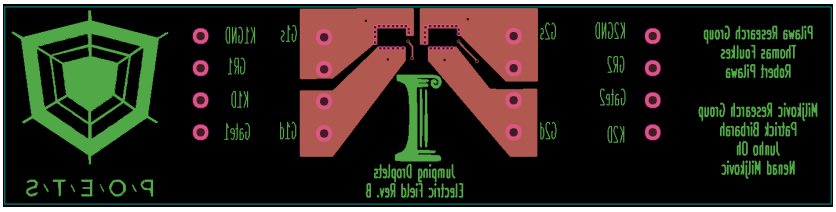

Figure A.6: PCB artwork for drill locations and for the back copper, back mask, and back silk layers of revision B.

APPENDIX B

LABVIEW PROGRAM

The thermocouple measurements were acquired using a National Instruments USB X Series Multifunction DAQ. Using a producer-consumer loop, data was sampled and stored to an Excel file for post-processing. The voltage and current settings of the Agilent E3631 and HP6033A power supplies can also be updated in real-time using an event structure within the main while loop of the consumer loop. Both DAQmx and NI 488.2 (at least version 15) are required to provide the drivers for LabVIEW to acquire data from the DAQ device. The front panel display is depicted in Fig. B.1.

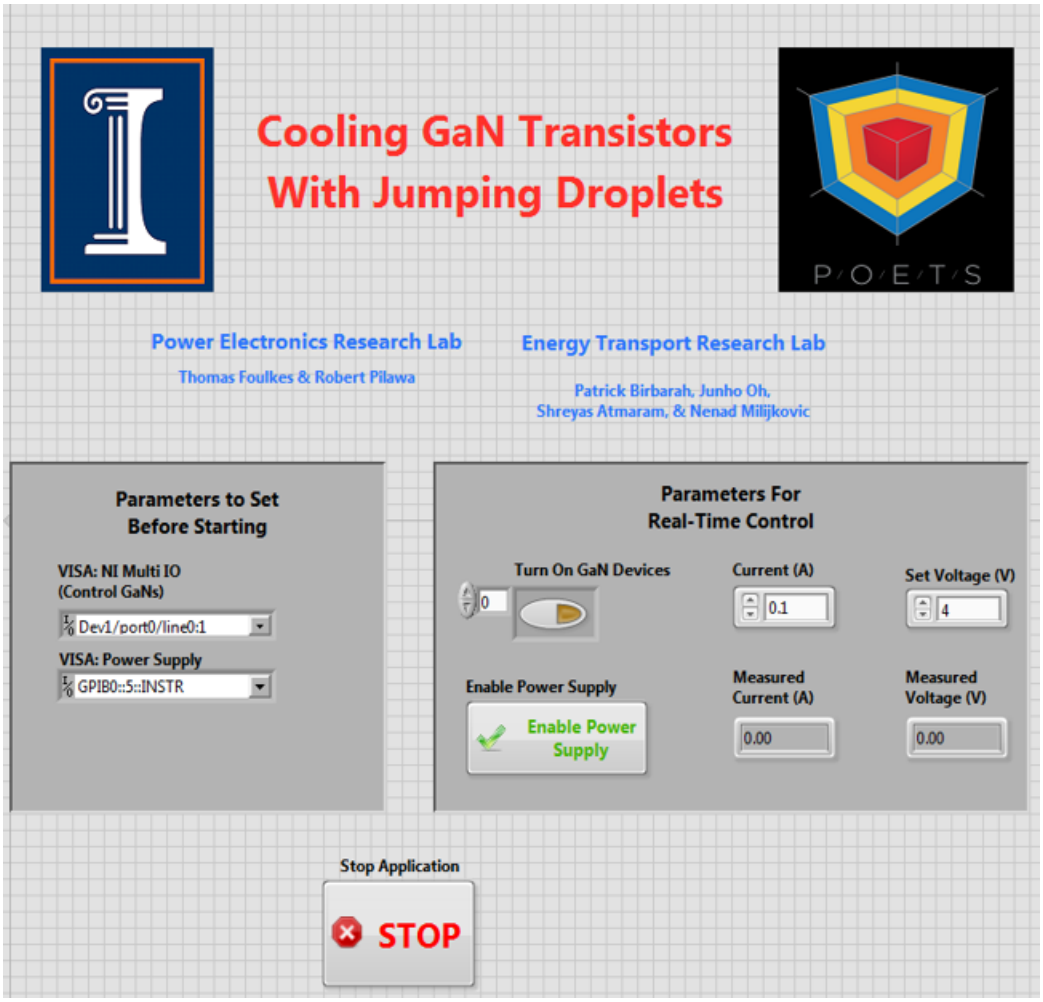

Figure B.1: Front panel of LabVIEW program.